**FACULTY
OF MECHANICAL
ENGINEERING
CTU IN PRAGUE**

Department of Energy Engineering

Ohřev experimentálního vzorku hypervapotronu

Heating of the experimental sample of the hypervapotron

MASTER'S THESIS

2022

Bc. Marek Dominik PAVELEC

Study program: N3951 Nuclear Power Device
Field of study: 3907T011 Nuclear Power Device
Supervisors: Ing. Pavel Zácha, Ph.D.
                  Ing. Miroslav Gleitz

MASTER'S THESIS ASSIGNMENT

I. Personal and study details

Student's name: **Pavelec Marek Dominik**   Personal ID number: **476076**

Faculty / Institute: **Faculty of Mechanical Engineering**

Department / Institute: **Department of Energy Engineering**

Study program: **Nuclear Power Device**

Branch of study: **Nuclear Power Device**

II. Master's thesis details

Master's thesis title in English:

Heating of the experimental sample of the hypervapotron

Master's thesis title in Czech:

Ohřev experimentálního vzorku hypervapotronu

Guidelines:

Bibliography / sources:

Name and workplace of master's thesis supervisor:

Ing. Pavel Zácha, Ph.D.   Department of Energy Engineering FME

Name and workplace of second master's thesis supervisor or consultant:

Ing. Miroslav Gleitz   Department of Energy Engineering FME

Date of master's thesis assignment: **21.04.2022**   Deadline for master's thesis submission: **03.06.2022**

Assignment valid until: **31.12.2023**

_____   _____   _____
Ing. Pavel Zácha, Ph.D.   Head of department's signature   doc. Ing. Miroslav Španiel, CSc.
Supervisor's signature   Dean's signature

III. Assignment receipt

The student acknowledges that the master's thesis is an individual work. The student must produce his thesis without the assistance of others, with the exception of provided consultations. Within the master's thesis, the author must state the names of consultants and include a list of references.

_____   _____
Date of assignment receipt   Student's signature

Declaration

I hereby declare that I completed this thesis independently with help of my supervisors. I used only resources and literature listed in the table of bibliography.

In Prague …………………………   …………………………………………….

Bc. Marek Dominik Pavelec

Acknowledgements

I would like to thank my thesis supervisors, Ing. Pavel Zácha, Ph.D. and Ing. Miroslav Gleitz, for their consultations, feedback, and support. Also, I would like to thank Ing. Jaroslav Plešinger for support with Ansys software and my family for their patience and support during my studies.

Annotation List

Author name:	Bc. Marek Dominik PAVELEC
Název práce:	Ohřev experimentálního vzorku hypervapotronu
Thesis name:	Heating of the experimental sample of the hypervapotron
Year:	2022
Study program:	N3951 Nuclear Power Device
Field of study:	3907T011 Nuclear Power Device
Department:	Department of Energy Engineering
Supervisors:	Ing. Pavel Zácha, Ph.D. Ing. Miroslav Gleitz

Bibliographical information:		
	Number of pages:	69
	Number of figures:	53
	Number of tables:	11
	Number of appendices:	0

Klíčová slova:	Jaderná fúze, tokamak, chlazení vysokých tepelných toků, hypervapotron, indukční ohřev, Ansys Maxwell
Keywords:	Nuclear fusion, tokamak, high heat flux cooling, hypervapotron, induction heating, Ansys Maxwell
Anotace:	Diplomová práce se zabývá návrhem ohřevu experimentálního vzorku hypervapotronu. Rešerše popisuje současný stav technologií chlazení vysokých tepelných toků pro jadernou fúzi a jak hypervapotron jako jedna z takových technologií funguje. Praktická část se skládá s analýzy problematiky a simulací indukčního ohřevu v programech Ansys. Validace výsledků bude provedena v nadcházejícím výzkumu.
Abstract:	Master's thesis deals with the design of the heating of the experimental sample of hypervapotron. The research part describes the current state of high heat flux cooling technologies for nuclear fusion and how hypervapotron as one of such technologies works. The practical part consists of assignment analysis and simulations of induction heating in Ansys programs. Validation of the results will be done in further research.

Table of Contents

List of Figures

List of Tables

Acronyms

AC	Alternating Current
BB	Breeding blanket
BESTH	Beryllium Sample Thermal Testing
CAD	Computer Aided Design
CFD	Computational Fluid Dynamics
CTU	Czech Technical University
DEMO	DEMOnstration power plant
EAST	Experimental Advanced Superconducting Tokamak
EM	Electromagnetic
ESS	Energy Storage System
EU	European Union
FEM	Finite element method
HCPB	Helium Cooled Pebble Bed
HELCZA	High Energy Czech Load Assembly
HHF	High Heat Flux
HTC	Heat Transfer Coefficient
HV	Hypervapotron
ITER	International Thermonuclear Experimental Reactor
IVT	Inner vertical target
JET	Joint European Torus
KoHLT	Korea Heat Load Test Facility
OVT	Outer vertical target
PCS	Power Conversion System
PHTS	Primary Heat Transfer System
RP	Reflector plate
WCLL	Water Cooled Lithium Lead

Symbols

Cp	[J/(kg.K)]	Specific heat
$\bar{H}$	[A/m]	Average magnetic field
HTC	[W/(m.K)]	Heat transfer coefficient
I	[A]	Electrical current
I_L	[A]	Induced electrical current
p	[Pa]	Pressure
P	[W]	Power
P_L	[W]	Power loss
R	[Ω]	Ohmic resistance
T_{in}	[°C]	Inlet temperature
T_{out}	[°C]	Outlet temperature
V	[V]	Electrical voltage
ε	[F/m]	Permittivity
μ_0	[H/m]	Vacuum permeability
$\overline{\mu_r}$	[H/m]	Average relative permeability
σ	[S/m]	Conductivity
ω	[Hz]	Angular frequency

1 Introduction

Humanity needs more energy as it develops in time. However, the current energy mix predominantly utilizes fossil fuel burning, which produces carbon dioxide. This gas is not toxic, but it is one of the greenhouse gases responsible for global warming. Therefore, the usage of the same fossil fuel technology is not sustainable. Alternative fossil-free sources already provide us with cleaner energy but not all of them can cover the rising demand and substitute fossil fuels at the same time. One of the ways could be the use of nuclear energy. Nowadays, only nuclear fission power plants generate energy.

Nuclear fusion is the process in which two light nuclei are forced together to form a larger nucleus, releasing a large amount of energy (the process powers the stars). This process can be replicated on Earth in a device known as a tokamak. A toroidal vessel and powerful magnetic fields are used to confine a hot plasma, allowing it to be heated to the conditions required for fuel fusion (currently these are Deuterium and Deuterium or Deuterium and Tritium, isotopes of Hydrogen).

JET, the Joint European Torus, is the world's largest operational tokamak and is based in Culham, Oxfordshire. JET and its successor ITER, International Thermonuclear Experimental Reactor (currently being built in Cadarache, France), provide critical steps toward developing a Fusion Power Plant DEMO (DEMOnstration power plant), which is expected to be completed in 2060'.

Tokamak plasmas, which lack the huge pressures generated by gravitational forces in stars, require extremely high temperatures (typically 100 to 200 million °C) to achieve the necessary conditions. When these conditions are combined with the output fusion power, heat fluxes of up to 10 to 20 MW/m^2 must be dissipated in both the tokamak and the auxiliary heating systems. The tokamak's divertor and first wall, are among the most heavily loaded components in a fusion reactor. To put this in context, these heat fluxes are typically an order of magnitude greater than those experienced in fission reactors.

2 High Heat Flux Cooling in Nuclear Fusion Reactors

2.1 First Wall

The first wall (Figure 1) has one specific feature compared to other cooling systems. Unlike original tokamaks, the breeding material for tritium production will have to be present for a sustainable fusion reaction. This makes the Primary Heat Transfer System (PHTS) even more complicated. The function of the coolant and the breeding material cannot be fully separated, as the breeding material also absorbs thermal energy and still needs to be cooled. The heat contained in the coolant is then transferred through Energy Storage System (ESS) to Power Conversion System (PCS) via a steam generator or heat exchanger to the medium that powers the turbine and generates electricity.

Several breeding blanket (BB) concepts have been proposed for future applications. Though, only two of them, HCPB (Helium Cooled Pebble Bed) and WCLL (Water Cooled Lithium Lead) are developed for the EU DEMO power plant [1] and will be tested in ITER. Both use reduced activation steel, EUROFER97, as a structural material [2].
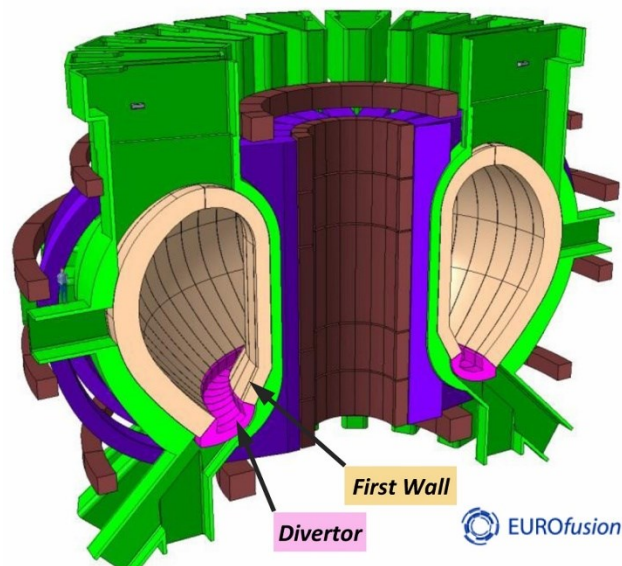
Figure 1: First wall and divertor in 2015 EU DEMO design [3].

2.1.1 HCPB

HCPB, Helium Cooled Pebble Bed (Figure 2), uses helium for cooling. The breeding part consists of Li_4SiO_4 (breeder material) and Be (neutron multiplier) beds which are separated by cooling plates. These are cooled by two parallel symmetric He flows. Helium is operated at p = 8 MPa, T_{in} = 300 °C and T_{out} = 500 °C [4].

This design simplifies the previous HCPB concept (as described in [5]) and improves performance [4].
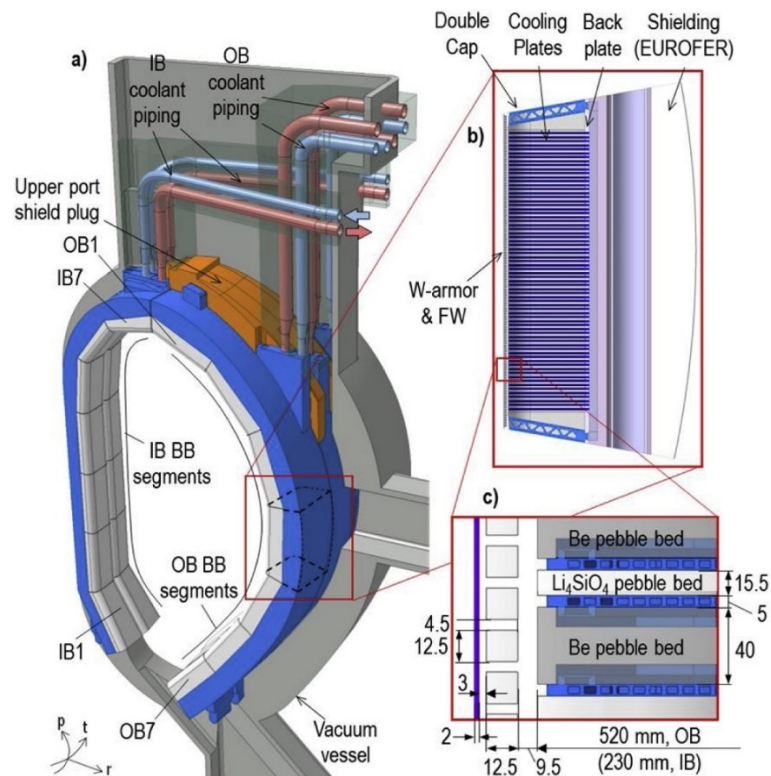
Figure 2: DEMO HCPB design [2]: a) elevation view; b) blanket toroidal cross-section; and c) detail of the breeding part.

2.1.2 WCLL

WCLL, Water Cooled Lithium Lead, uses water for cooling at Pressurized-Water-Reactor conditions which mean p = 15.5 MPa and T = 295-328 °C. Its breeding blanket is cooled by the first wall (Figure 3) and the independent breeding zone cooling systems. The first-wall cooling system can safely remove the plasma heat flux of 1.17 MW/m^2.

Breeding, neutron multiplication and tritium carriage are provided by Lithium-Lead (PbLi) which slowly flows radially through the breeding cells (Figure 4) [2].
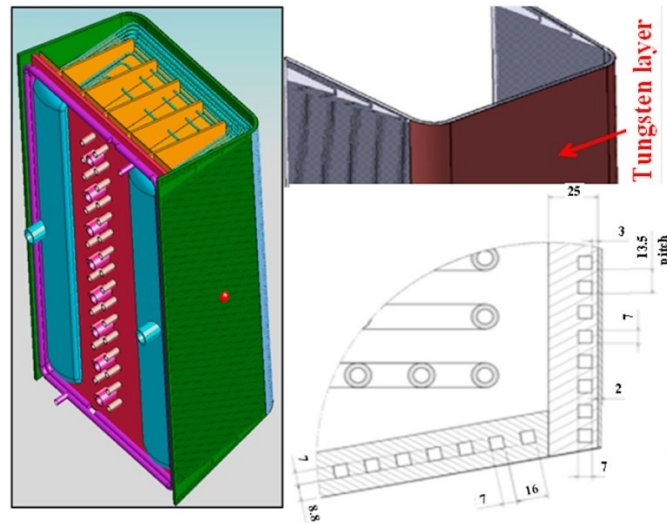
Figure 3: WCLL design with the detail of the first wall [6].
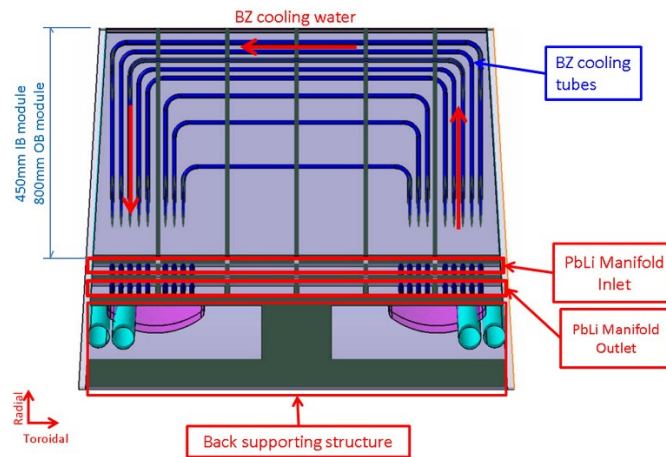
Figure 4: WCLL design – breeding zone detail [7].

2.2 Divertor

Divertor is a part of the tokamak that is subject to the highest loads in terms of heat flux. This part removes impurities and thus helps to keep the plasma clean. The magnetic field in this area directs impurities from the vacuum vessel to the vertical targets, where they are trapped and further discharged away. It is assumed that the maximum power density on the targets will reach approximately 20 MW/m^2 during transients in 2-3 seconds and 1-10 MW/m^2 during steady state operation [8]. The cooling of the divertor is therefore much more complex than for the first wall.

The common cooling systems cannot manage these loads and therefore new cooling methods are developed to increase the heat transfer coefficient.

Boiling is commonly mentioned in connection with heat flux removal. The simple principle is to create obstacles in the water flow that locally slow down the flow and due to the high heat flux, evaporation and subsequent condensation occur, which has a large impact on the heat transfer. There are many geometries and ways to achieve this phenomenon. Chang [9] lists (Figure 5): a round tube with a twisted tape insert (swirl tape), a round tube with a helical coil insert, a ribbed tube and a rectangular channel with a hypervapotron, which seems to be promising and will be described deeper in the following part.

(a) Round tube with a twisted tape insert

(b) Rectangular channel with a hypervapotron

(c) Round tube with a helical coil insert

(d) Ribbed tube
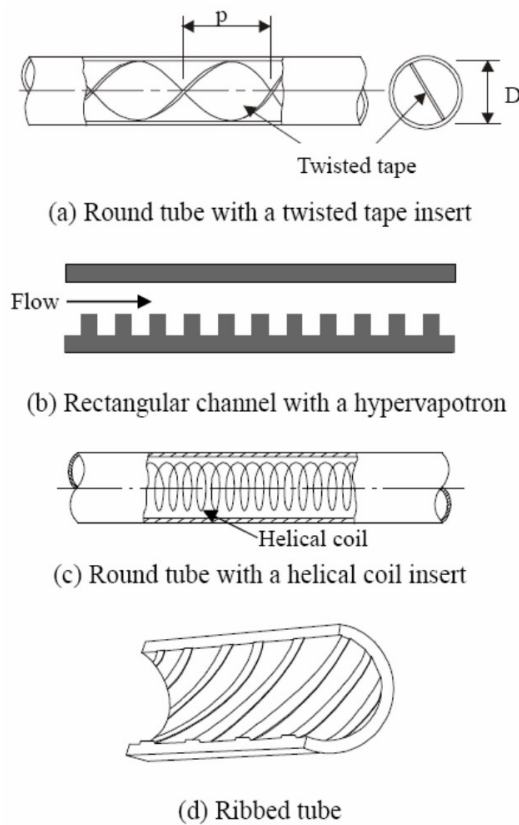
Figure 5: Chang's examples of High Heat Flux technology, (a) round tube with a twisted tape insert is also known as swirl tape [9]

Baxi [10] focuses on helium cooling and names relevant methods enhancing heat transfer: micro fins, porous media, jet impingement, particulate addition, swirl tape, 2D roughness, 3D roughness, swirl rod insert and swirl rod insert with 2D roughness. Helium

is a great coolant from the safety perspective as it is chemically and neutronically inert but 10 MW/m^2 may be an upper limit for the gas.

The disadvantage of these systems is the increase in pressure losses and thus the greater demands on pumping technology. Possibly the latest technology concept comes from Schwartz [11] who presented his Spiral Plate Module design (Figure 6) and managed to demonstrate a very low pumping ratio.
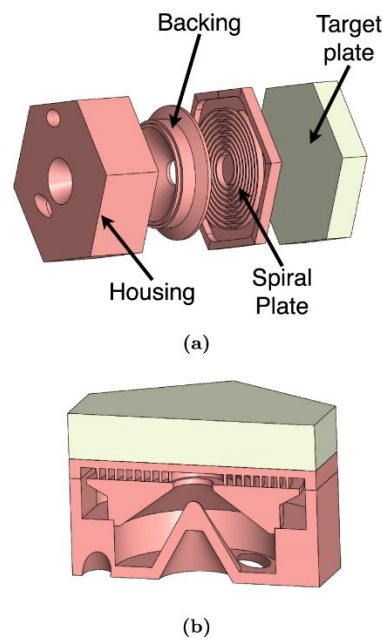
Figure 6: Schwartz's Spiral Plate Module. (a) assembly view, (b) cross-sectional view [11]

ITER uses water-cooled tungsten monoblocs as the divertor cooling system [12].

According to the 2020 DEMO concept, the tokamak's divertor (Figure 7) consists of a cassette body, a shielding liner, two reflector plates, and two vertical targets (the inner and outer ones). These are assembled from water-cooled tubes with swirl tapes inside, which improve heat transfer [13]. The divertor for the DEMO power plant will be water-cooled because the high heat flux conditions on the divertor surface are beyond helium cooling capabilities [2].
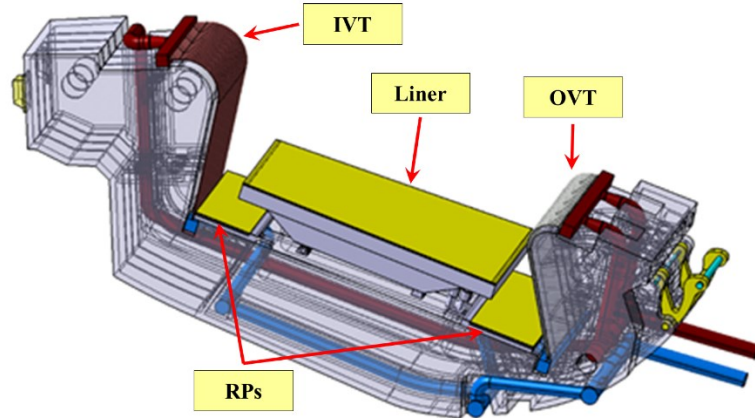
Figure 7: 2020 DEMO Divertor Assembly consisting of a cassette body, a liner, two reflector plates (RPs), an inner (IVT) and an outer vertical target (OVT) [13]

During the pre-conceptual research and development phase of DEMO, the five water-cooled target designs (Figure 8) were developed. Four of them were made of tungsten mono-block on a copper cooling pipe, while the last one had a tungsten flat tile on a copper composite cooling block. The designs were as follows:

- W mono-block joined with a CuCrZr cooling pipe and a Cu interlayer ("ITER-like"),
- W mono-block joined with a CuCrZr cooling pipe and a Cu thermal break interlayer ("Thermal break"),
- W mono-block with a W wire-reinforced Cu composite pipe ("Composite pipe"),
- W mono-block joined with a thin (20 μm) or thick (500 μm) functionally graded W/Cu interlayer ("FGM interlayer"),
- W flat tiles with a W particle-reinforced Cu composite heat sink block ("Composite block") [14].
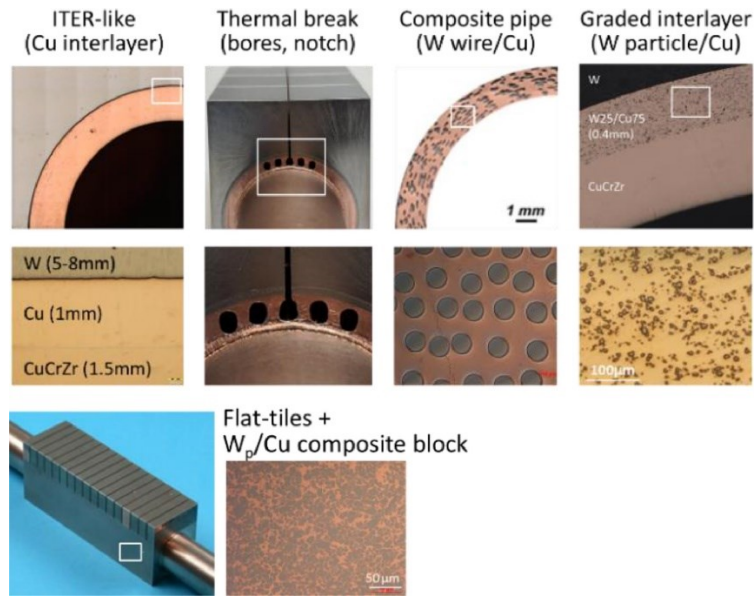
Figure 8: Design features of the DEMO divertor target concepts [14].

2.3 Hypervapotron

Hypervapotron (Figure 9) is one of the most promising devices among high heat flux (HHF) technologies. It is a channel with internal fins perpendicular to the water flow which allows water to boil and therefore intensifies the heat transfer [15].
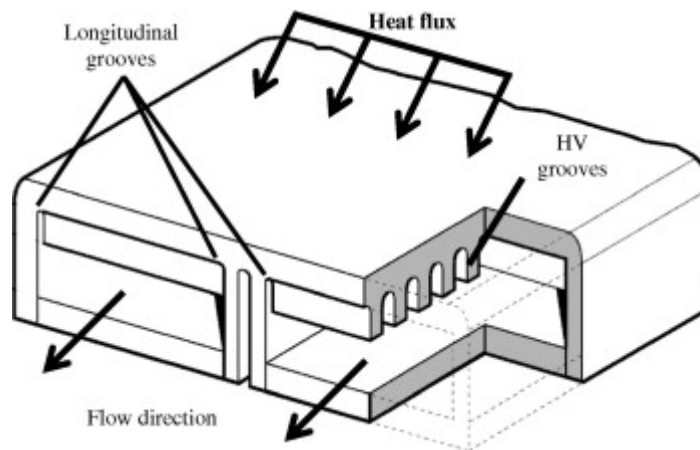
Figure 9: Hypervapotron channel design with a cutout showing fins [16].

2.3.1 Principle of operation

The hypervapotron's design makes use of fins of various diameters and shapes (Figure 10) that are positioned parallel to the coolant flow (e.g. water). The coolant evaporates among these fins (Figure 11) and condensates as soon as it enters the main

flow. This is subcooled boiling, which means the main flow temperature is below the saturation temperature. Heat transfer depends on the flow parameters, coolant choice, subcooling temperature and channel geometry. The temperature profile on fins is limited by the Leidenfrost temperature[1] at the root and allowed to exceed the initial boiling temperature at the fin tip [15].

Like this, the hypervapotron outperforms other cooling systems that utilize single-phase fluid flow in terms of efficiency [17].
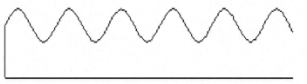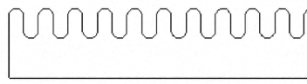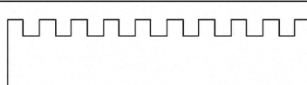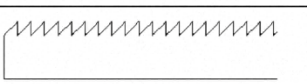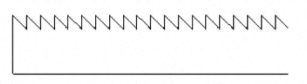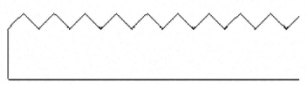
Number	Fin shape	Configuration
1	Sin curve	
2	Rectangle with fillet	
3	Rectangle	
4	Triangle to the flow direction	
5	Triangle against the flow direction	
6	Right -angle triangle	

Figure 10: Table of various fin shapes [18].

---

[1] The temperature when the evaporation time is the longest and the boundary between transition boiling and film boiling of liquids.
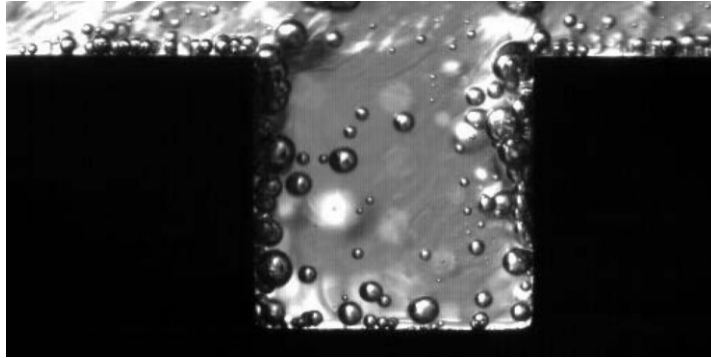
Figure 11: Evaporation in HV-like groove [19].

2.3.2 Material

So far, copper has been used as the basic material in hypervapotron, which appears to be suitable in terms of properties, particularly because of its high thermal conductivity. The most common building material is CuCrZr, a hardened copper alloy with high strength and hardness as well as the previously mentioned high electrical conductivity. Copper is the most abundant element in this material (more than 99 %), with chromium (0.8 %) and zirconium (0.08 %) being the least abundant. According to Ciric [20], the maximum surface temperature load for this alloy is 450 °C.

2.3.3 History

The origin of hypervapotron is in vapotron technology, which was industrially applied since the 1950s. Beutheret [21] described the Vapotron Effect (1-2 in Figure 12) as a stabilized boiling process along a non-isothermal wall with fins, where the fin tip is below the boiling temperature and the fin root has a temperature safely below the Leidenfrost temperature. He further proposed a supervapotron design with fins located parallel to the main flow. For this design, the fin root temperature is close to the Leidenfrost limit and the fin tip exceeds the boiling temperature (3-4 in Figure 12).
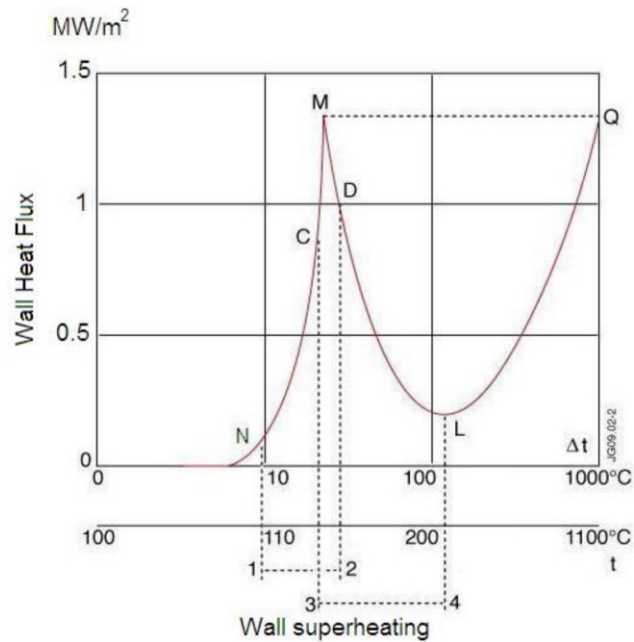
Figure 12: Boiling Curve of Vapotron (1-2) and Supervapotron (3-4) [15].

As it seems, the supervapotron's fins were parallel to the flow which did not enter the grooves. For that reason, Beutheret proposed to orientate the fins perpendicularly to the flow and a hypervapotron was born.

It was further developed and only in 1980 appeared in a fusion-related report for the first time. A French company Thompson CSF studied a rectangular design for the JET's actively cooled beam dumps of Neutral Beam Injection system [22].

2.3.4 Advantages compared to others

The hypervapotron seems to be one of the potential methods for removing the high heat fluxes from fusion reactor components. Compared to so far examined cooling devices (swirl fins, swirl tapes, porous coatings, …), the hypervapotron has a greater critical heat flux limit and lower pressure drop which means lower pumping power [15].

2.3.5 Experiments with HV

This chapter presents previous publications on hypervapotron experiments. The goal is to get to know the experimental devices and specifically the heating methods which were used.

Cattadori G. (1993) – Hypervapotron Technique in Subcooled Flow Boiling CHF

The work focuses on the hypervapotron effect and the related heat transfer phenomena as a function of geometry and fluid thermal hydraulic conditions. The geometry of the hypervapotron itself is tubular with external ribs and it is placed in a transparent tube allowing camera use.

The circuit diagram of the test loop is shown in Figure 13.
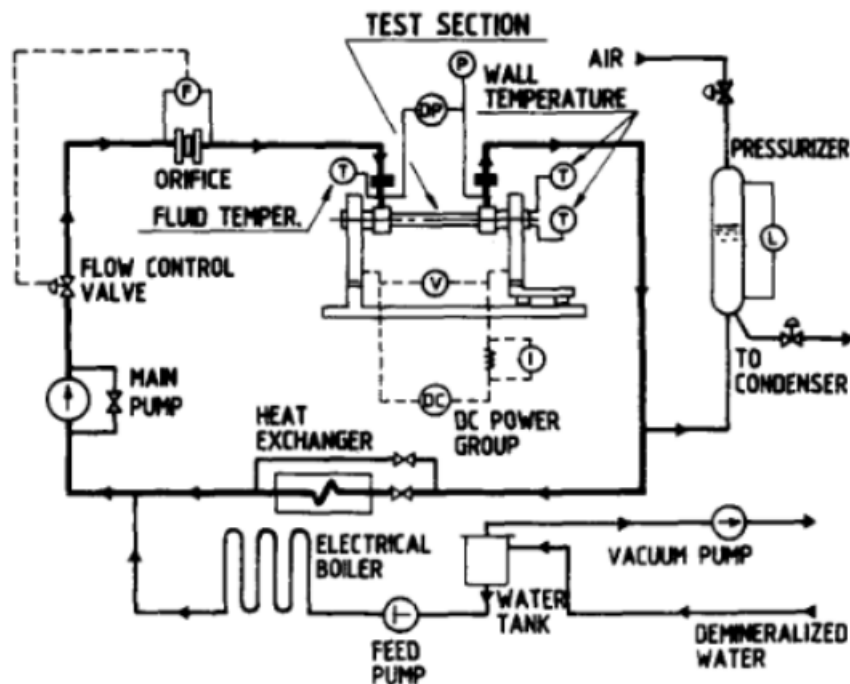
Figure 13: Scheme of Cattadori's test loop

Heating applied to the hypervapotron works on the ohmic heating principle. The direct current source is connected to power lugs as shown in Figure 14 and provided a maximum of 50 kA and 160 V.

Figure 14: Drawing of the test section

The achieved peak critical heat flux in this hypervapotron was 29.4 MW/m^2 for 7 mm high and 2 mm wide fins with 2 mm gaps. The used pressure was 0.9 MPa, velocity 9 m/s, inlet temperature 60 °C and subcooling temperature difference 115 °C [23].

Escourbiac F. (2003) Experimental optimisation of a hypervapotron concept for ITER plasma facing components

This thesis checks the dependence of critical heat flux on the hypervapotron channel width (to help the research of plasma-facing components for ITER). An important finding is that critical heat flux decreases with increasing width.

Samples were manufactured from Glidcop AL25 (Al$_2$O$_3$) and tested in various conditions [24].

Figure 15: Section view of the tested design

Figure 16: Opened hypervapotron channel HV40-1

As a heating source, a 200kW electron beam gun at European high heat flux facility FE200 is utilized for this experiment. It was built in 1991 to test the plasma-facing components under heat fluxes from 0.1 MW/m^2 to more than 100 MW/m^2. A vacuum testing vessel allows analysing devices connected to a cooling system – a water pressurized loop operating at 0.2-3.3 MPa, 50-230 °C. More details are available in ref. [25].

A removed peak heat flux of up to 25-30 MW/m^2 with an axial velocity of 4-6 m/s was observed during these experiments [24].

Chen P. (2007) Heat transfer characteristics in subcooled flow boiling with hypervapotron

Chen conducted an experimental study of subcooled boiling heat transfer with R-134a in a cartridge-heated hypervapotron device. The hypervapotron fins he used are consistent with Baxi's [26] and Cattadori's [23] design - fin height 3 mm, fin width 3 mm, fin pitch 6 mm. For heating, Chen used seven cartridge heaters (Figure 18) with a total power of 5.25 kW which were inserted from the bottom of the test section.

Two characteristic boiling zones were identified during the boiling process in the hypervapotron. Compared to the flat channel, the hypervapotron design increased the critical heat flux by 40-50 %. The maximum achieved heat flux was approximately 850 kW/m^2 [27].
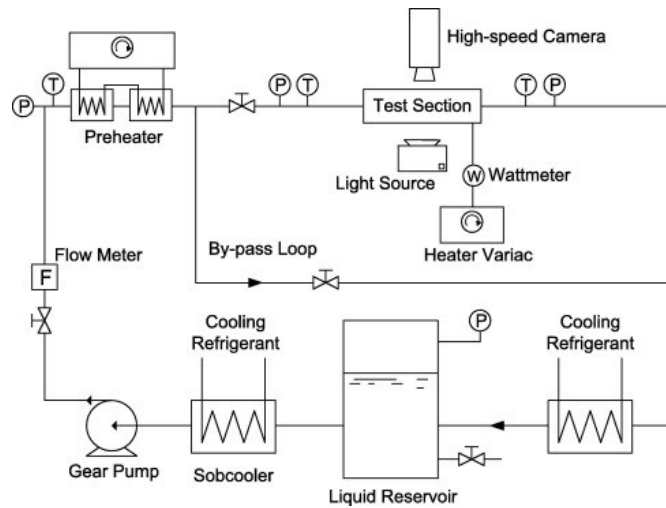
Figure 17: Scheme of Chen's test loop [27].
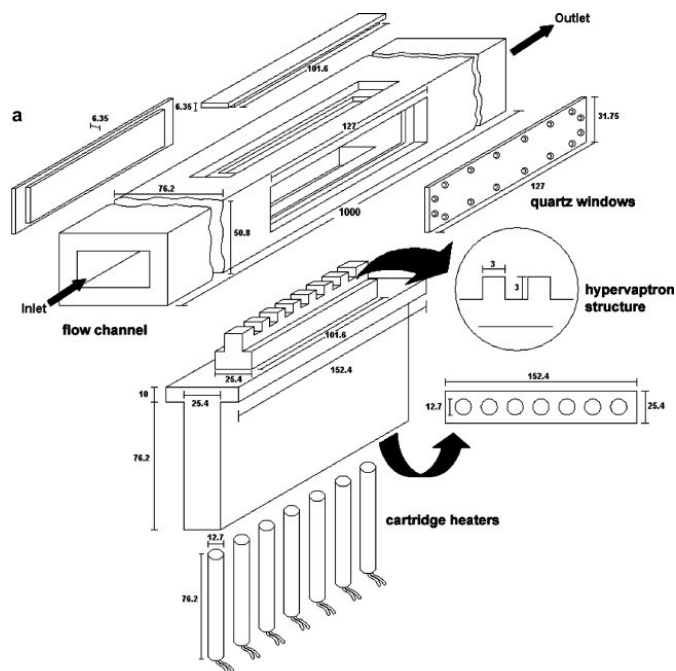
Figure 18: Test section diagram [27].

2.3.6 Experimental loop

Gleitz [28] designed and built an experimental loop in the Energetics laboratory at Czech Technical University (CTU) in Prague to analyse real subcooled boiling mechanisms in hypervapotron. This thesis is mostly based on the need for sufficient

heating of that hypervapotron and therefore the geometry and boundary conditions that result from it.

The loop scheme is pictured in Figure 19. It starts with the hypervapotron channel (1), which is heated by the heat flux source (2). Behind the channel, there is a safety valve (3), followed by an expansion tank (4) and an induction flow meter (6). In the lowest point of the loop, a filling/draining valve (5) is located. After the valve, water goes through an electric boiler (7) which ensures the desired water temperature in the loop. Then, a water pump (8) with a reverse bypass regulates the water flow. Before water enters the hypervapotron channel again, it is cooled by a cooler (9) to precisely reach the desired temperature.
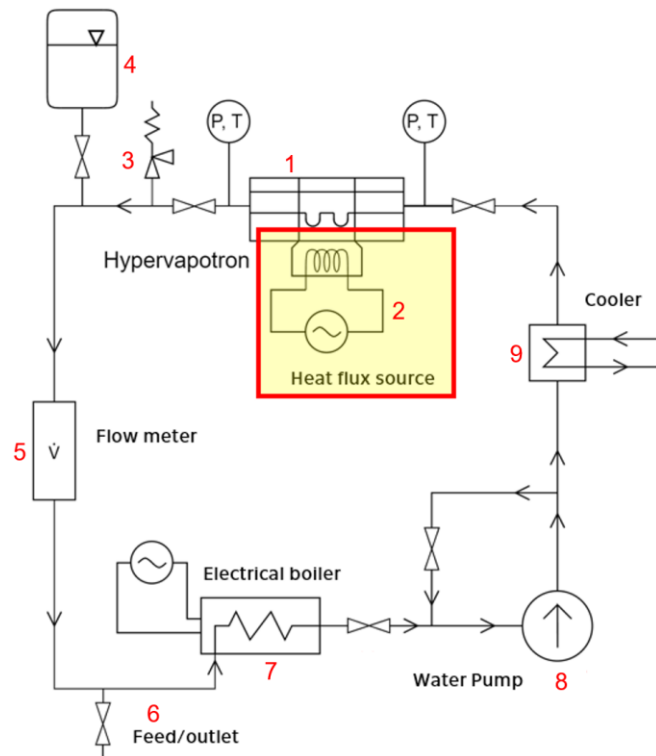
Figure 19: Gleitz's hypervapotron experimental loop with highlighted heat flux source

The loop operation is controlled by pressure, temperature, and flow at the inlet to the channel.

Hypervapotron channel parts are manufactured from the stainless steel AISI 304, 1.4301 because of its low thermal conductivity (~10-30 W/(m.K)) and corrosion resistance. Sealing and thermal insulation between the hypervapotron and the channel is secured by plates of Klingersil C4400.

The hypervapotron itself is made of CW106C (CuCrZr) alloy whose material properties are very similar to pure copper.
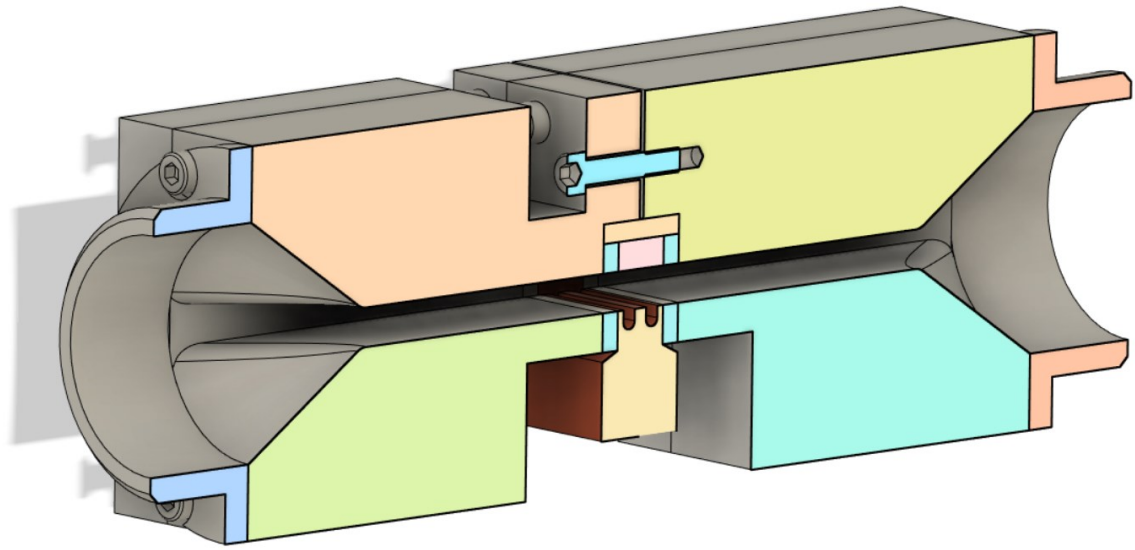
Figure 20: CAD design: Section view of hypervapotron channel test section without the coil.

3 Assignment Analysis

3.1 Description

The goal is to provide high heat flux to the hypervapotron sample instead of the high heat flux coming from plasma. Some of the tokamak's components are expected to be exposed to up to 20 MW/m^2 heat flux which is a good reference and the best target for the heating.

3.2 Heating methods

In common laboratory conditions, a working fusion reactor is not available, but a few different heating methods listed below could be used instead.

3.2.1 Ohmic heating
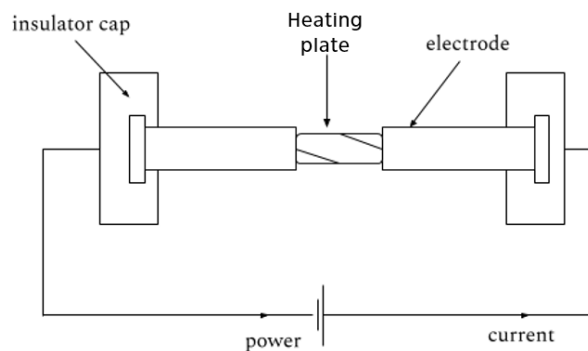
Figure 21: Ohmic heating diagram

The ohmic heating method generates heat by current flowing through a heating plate. The following formula describes the heating power:

$$P = I\,(V_a - V_b),$$

where P is power, I is current and $V_a - V_b$ is the voltage drop across the plate.

SIET labs achieved heat fluxes of up to 30 MW/m^2

Graphite heater

Graphite heating works on the same principle; however, graphite is used as a resistor generating lower heat fluxes – about a few MW/m^2.
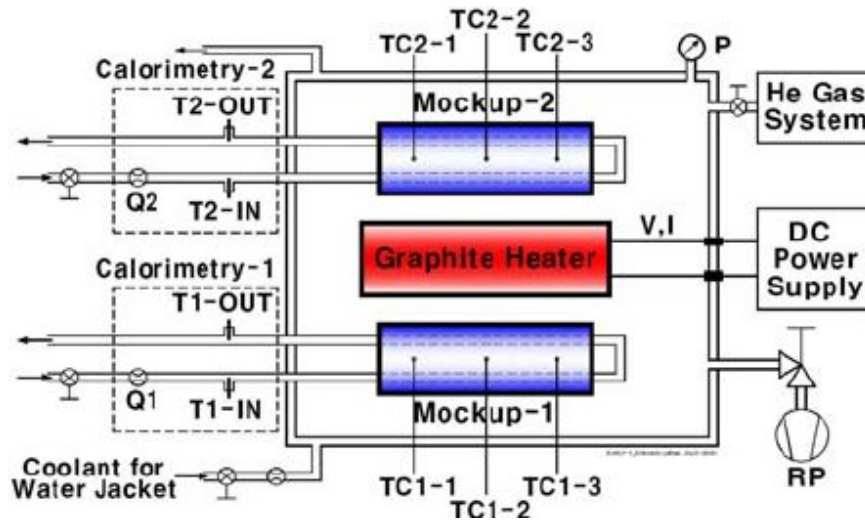
Figure 22: Graphite heater diagram

This system has been demonstrated in the BESTH facility, TW3 and in Korea on a KoHLT-1 project [29].

Cartridge heating

Cartridge heating makes use of the ohmic heating principle. The heating loop is incorporated into a cartridge. This method can reach heat fluxes up to 1 MW/m^2. One of the studies which used this design is briefly described in chapter 2.3.5.
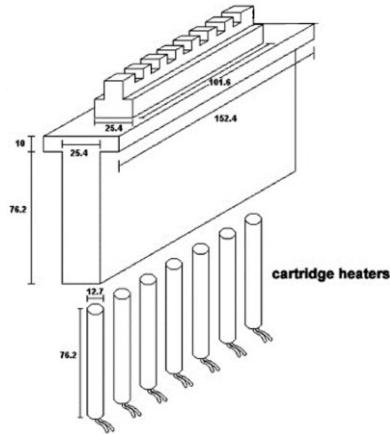
Figure 23: Cartridge heating diagram [27].

3.2.2 Ion and electron beam guns

Ion and electron beam guns emit charged particles which generate heat while colliding with the surface. Their heating power ranges from watts to a few megawatts. Out of the mentioned methods, it dominates. On the other hand, the availability of beam guns is limited.

Many facilities with beam guns operate for years and some of them were specially built for testing plasma-facing components. One of those is the HELCZA facility (Figure 24) which was built to test the first wall panels for ITER by an electron beam. This specific beam gun can generate up to 40 MW/m^2 heat flux (20 MW/m^2 for unlimited cycles) [30].
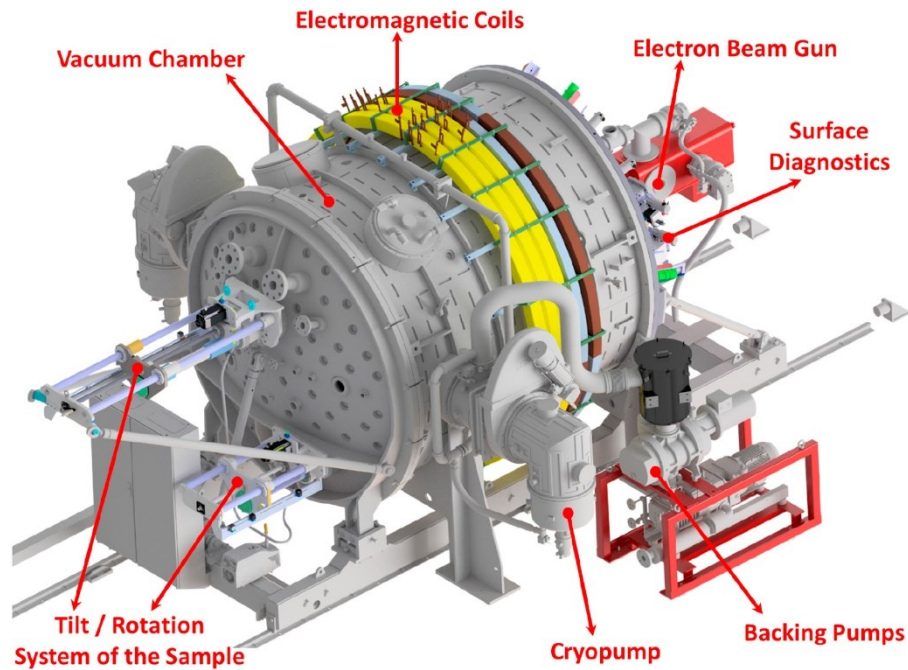
Figure 24: Main parts of HELCZA facility [30].

3.2.3 Induction heating

AC (Alternating Current) source supplies an alternating voltage to the coil and creates an alternating magnetic field surrounding the target object. That causes the object to heat in two ways: magnetic hysteresis losses and eddy current losses.
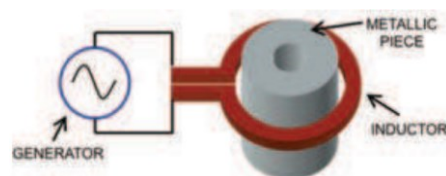
Figure 25: Scheme of an induction heating system in a longitudinal flux configuration

An eddy current is induced when there is a change in a magnetic field. This produces heat by Joule effect thanks to the current flowing through the core and it is the main heat source in induction heating. Hysteresis losses come from energy used for magnetic particle positioning in magnetic materials [31] [32].

Induction heating is fast, efficient, controllable, consistent, repeatable, clean, and safe. These advantages lead to wide industrial, domestic, and medical applications [32].

The maximal reported heat flux of 2 MW/m^2 generated by induction heating for the HV experiment was achieved while analysing an HV mock-up for EAST tokamak [18].

3.3 Analysis result

An induction heating method was selected because it seems to be a promising approach in our conditions. Also, it is easily available, unlike ion or beam gun machines.

The chosen system consists of an induction heater (Figure 26 and Table 1), a cooled induction coil and a core which will be heated. The used coil is displayed in Figure 28.

Figure 26: Induction Heater (U.S. Solid 15 KW High Frequency Induction Heater 30-80 kHz)

Table 1 Induction Heater – Main Characteristics

Input Voltage	Single Phase; 220 V or 110V
Max. Output Power	15 kW
Output Power	7 kW
Max. Heating Temperature	1200°C
Fluctuating Frequency	30 - 80 kHz
Fluctuating Heating Current	200 - 600 A
Thermal Insulation Current	200 - 600 A
Cooling Timing	1 - 99 s(Auto)
Thermal Insulation Timing	1 - 99 s(Auto)
Heating Timing	1 - 99 s(Auto)
Flow Rate of Cooling Water	7.5 l/min; 0.06 – 0.12 MPa

Lift of Cooling Water	≥ 30 m
Water Temp. Protection Point	40 °C
Net Weight	25 kg
Dimensions	550 x 220 x 470 mm

Initially conducted induction heating tests with a copper alloy block did not appear to be a working method. Therefore, the investigation started to simulate the induction and generated heat flux in the original geometry. Later, the copper alloy block will be altered and suggestions for improvements will be made.

4 Multiphysics simulation

This chapter describes the multi-physics simulation software including EM (electromagnetic) and CFD (Computational Fluid Dynamics) simulations. Ansys programs are used since CTU in Prague provides students with its license.

Ansys offers a huge variety of programs for most fields of engineering, e.g. programs for structure simulations (strength, elasticity, fatigue), fluid and gas flow analysis (heat transfer, particle flow, freezing/fogging simulations), optics, acoustics and other multiphysics calculations.

4.1 Ansys Electronics Desktop

Ansys Electronics Desktop is a platform that combines Ansys' electromagnetic apps into a single graphical user interface. The program connects high-frequency (Ansys HFSS, Ansys Savant, Ansys EMIT, Ansys Q3D), low-frequency (Ansys Maxwell, Ansys RMxprt, Ansys PExprt) and circuit (Ansys Nexxim, Ansys Simplorer and Ansys Twin Builder) simulation programs. The interconnection of programs also extends to the field of cooling, specifically the Ansys Icepak program.

Ansys Electronics Desktop's unified environment combines accurate electromagnetic analyses with frequently quite in-depth circuit-system simulations into a simple yet effective whole. Individual programs' wide range of solvers makes it possible to simulate extremely specific tasks and produce reliable results. It is possible to use simulations from Ansys Workbench, Ansys Simplorer, or Ansys Twin Builder for multi-physics solutions with other Ansys products.

Each program contains extensive libraries of materials and components that are constantly expanding. Script creation using Python or Visual Basic provides complete flexibility in design and resolution.

A program for making calculations in the area of low-frequency electromagnetic fields is called Ansys Maxwell. Simulations are run using the finite element method (FEM), which is generated adaptively. Both 2D and 3D can be used to solve problems involving rotating and non-rotating machinery. The software supports simulations in the time and frequency domain. Either a stationary or a non-stationary solution is possible.

The tool can be used to generate the solved geometry using predefined elements or it can import the geometry in CAD (computer aided design) format. Another approach is to link directly to the Ansys Maxwell license's Ansys RMxprt and Ansys PExprt programs. Solvers for electrostatic or electromagnetic simulations are available. The definitions of the materials used in the library consider their nonlinearities, temperature, and frequency dependences, eddy current effects, skin effects, demagnetization, magnetostriction, or amorphous features. The library supports any type of data export and import.

The program permits the solution of rotational and translational motion using time-dependent simulations. The program's Circuit Editor module is used to build a particular power supply. You can use the application to solve optimization problems by altering the input settings. The program can be used as an input for multi-physical calculations of an object's cooling or strength as well as for the design and solution of a specific machine [33].

4.2   Ansys Fluent

Ansys Fluent is a 2D / 3D computer fluid dynamics (CFD) simulation tool. Its characteristic feature is its versatile use from basic to physically complicated applications. It offers physical models focused on modelling flow, turbulence, heat transfer and chemical reactions for industrial applications – from airflow through aircraft wings and furnace combustion to bubble columns on oil rigs, from bloodstream simulation to semiconductor production or from the well-being of housing up to wastewater treatment plants. Fluent covers a wide range, including specialized models with aero-acoustics modelling capabilities, combustion in engine chambers, paddle machines and multiphase systems [34].

4.3   Ansys Workbench

All customers of Ansys products can use the free Ansys Workbench environment, which houses the full range of Ansys simulation programs. These include software applications like Ansys Fluent, Ansys CFX, Ansys Mechanical, Ansys Maxwell, etc. as well as specific tasks like geometry development, heat calculation, static analysis, etc.

The block architecture makes it very simple to connect individual blocks, share common data, generate different versions, and ultimately construct the full automated process out of various blocks in this environment.

The various technologies are shown here as blocks that may be readily engaged and connected by dragging the mouse. Flowcharts are then used to show projects as interconnected systems. Because of this, the purpose of the simulation, the connections between the data, and the stage of the project's analysis are all immediately clear. The structure of blocks and mouse dragging enables the user to create multidisciplinary analyses quickly and clearly while also guaranteeing automatic data flow, i.e. This transfer is automatically ensured between the pertinent simulations, such as between structural and current analysis.

All Ansys applications and solvers within this environment have access to the Ansys Workbench's ability to parameterize individual blocks [35].

5 Workbench setup

5.1 Workflow preparation

Geometry, Maxwell 3D and Fluent (with Fluent Meshing) systems are consecutively added to the blank canvas. Geometry acts as a source of CAD data for Maxwell 3D geometry and Fluent Meshing. Once Maxwell 3D analyses the simulation, the Maxwell 3D solution is connected to the Fluent setup to transfer the EM losses. Fluent maps them to its volumetric mesh and analyses the temperature profiles. The feedback Iterator tool is then used to create a loop between Fluent and Maxwell 3D. Fluent sends the simulated temperature data to Maxwell 3D which recalculates the losses according to the received temperature conditions and sends the updated EM losses to Fluent for another simulation. This loop runs until the average delta temperature of the geometries in Fluent between the two consecutive iterations gets below 5 %.
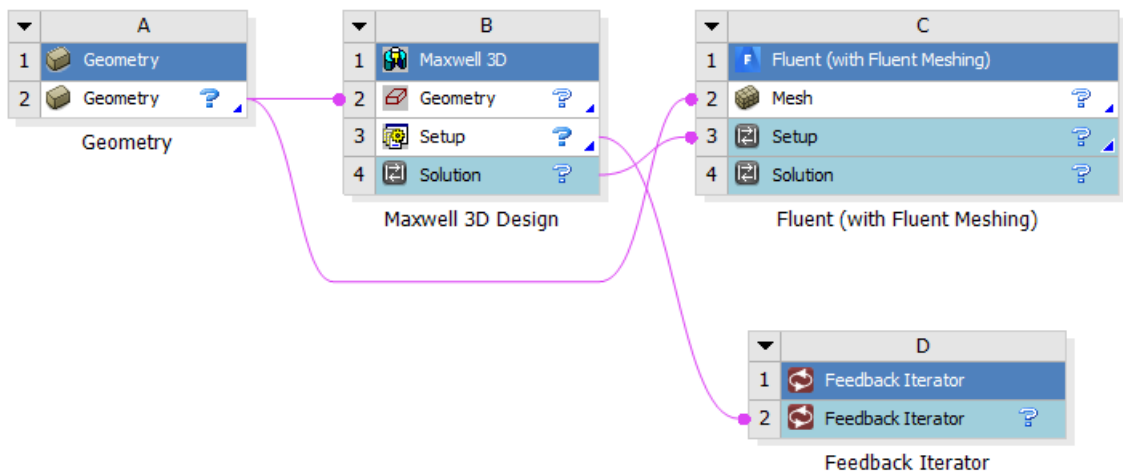
Figure 27: Workflow scheme in Ansys Workbench

5.2 Geometry

The hypervapotron sample is a part of the experimental channel and just the bottom part, is accessible to the heating source. It appears to be the easiest to manufacture a heated core with the hypervapotron sample as one piece but due to technical reasons, the heated core is connected by silver brazing. That should offer negligible heat transfer changes.

Three similar core geometries are going to be simulated with the same 3turn coil surrounding them. The heating coil is made of a 6mm tube which is bent to a rectangular shape creating inner space with dimensions 65x30 mm. Geometry #1 consists of an HV part and a core element. The HV part design comes from [17]. Geometry #2 has been improved by additional steel plates on the sides of the core which are expected to boost the total electromagnetic loss. Geometry #3 reflects the simulation results presented later. As both Geometry #1 and #2 had accumulated most of the EM loss on the bottom, the third geometry keeps the plates on the core and the entire core assembly is elongated in the vertical direction. CAD renders and dimensions are provided in the figures below.

Figure 28: CAD design of Geometry #1 with the coil
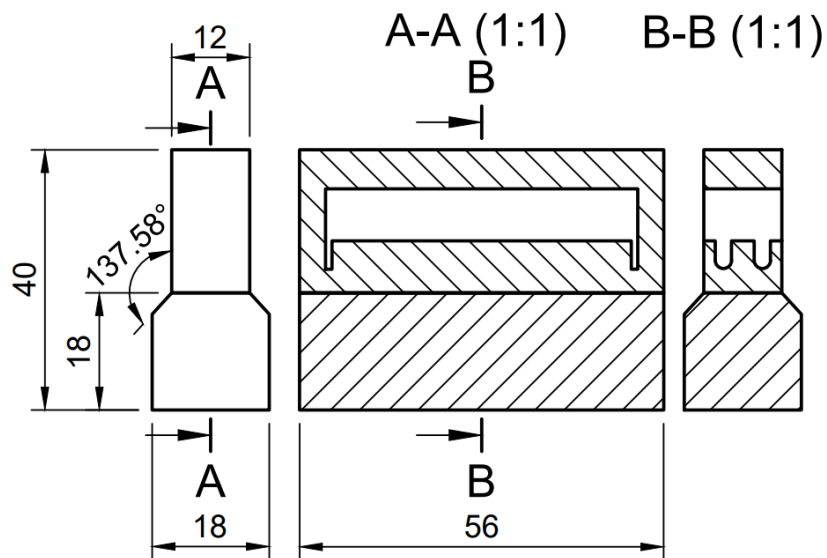
Figure 29: Geometry #1 dimensions
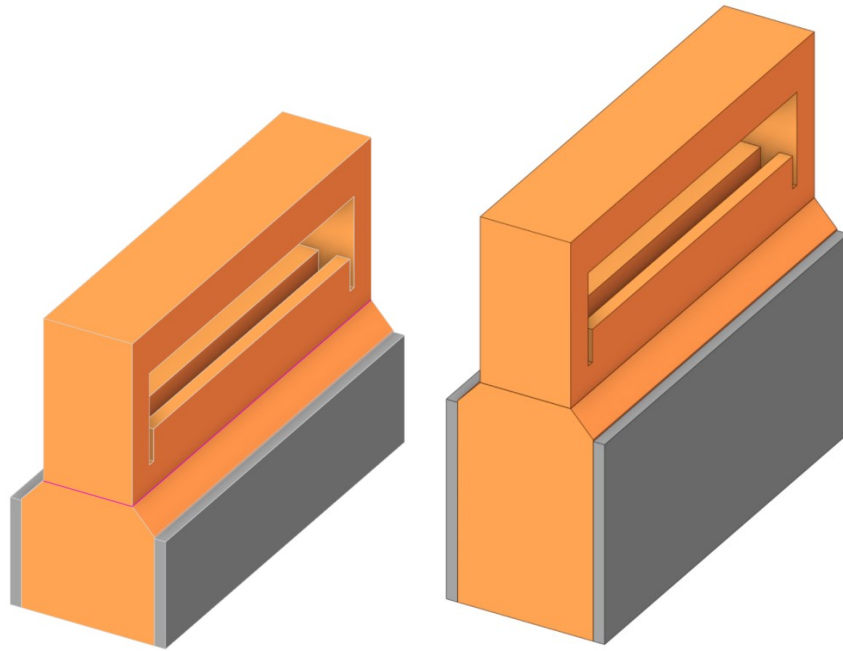
Figure 30: CAD designs of Geometry #2 and Geometry #3 without the coil
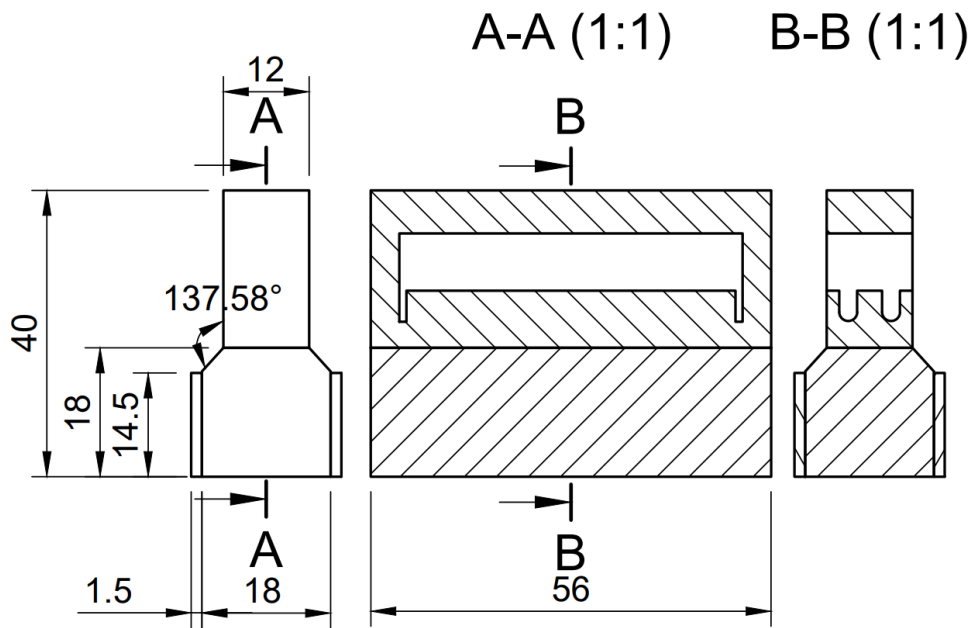
Figure 31: Dimensions of Geometry #2

A-A (1:1)   B-B (1:1)

12

A

137.58°

52

30

26.5

B

A

1.5   18

B

56
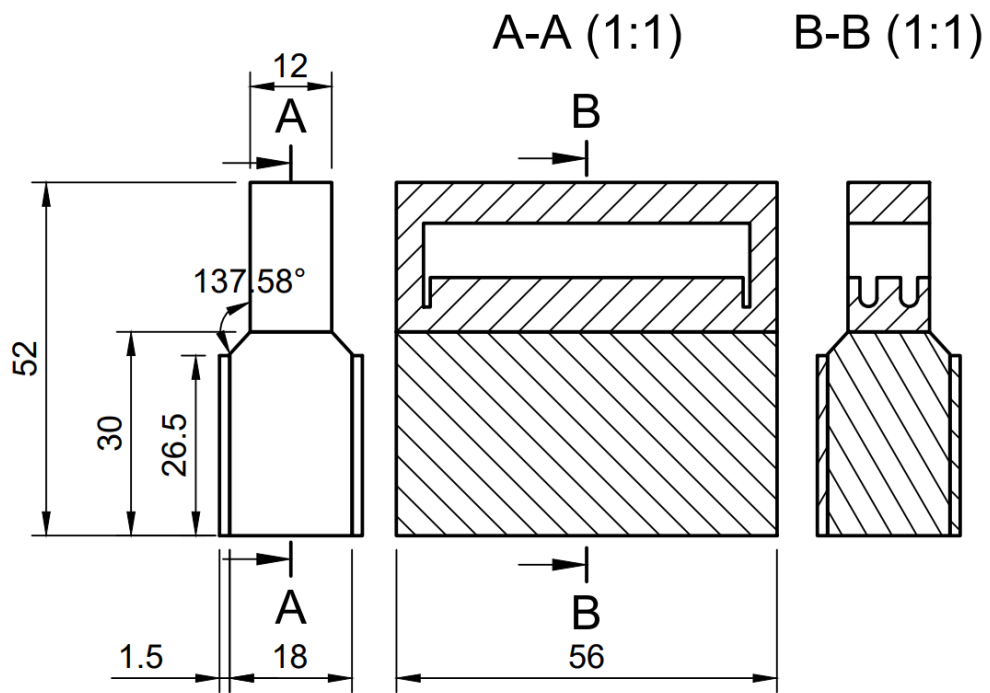
Figure 32: Drawing of Geometry #3

6 Maxwell setup

After importing the geometry, a region surrounding the objects is created so that a magnetic field has space to develop during the simulation. The region has 50% offset padding in all dir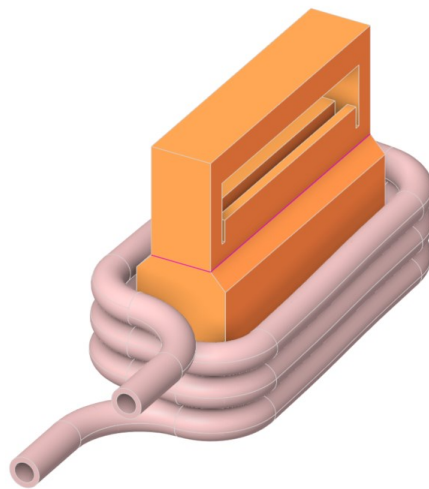ections except for the one where the coil ends. There it has 0% padding because of the excitation which will be assigned later.

6.1 Solver type

The purpose of the simulation is to simulate excitation by an alternating current in the coil creating a magnetic field. Therefore, the *"Eddy Current"* solver will be used. This solver computes steady-state, sinusoidal magnetic fields at given frequencies from the equation

$$\nabla \times \left[\frac{1}{\sigma + j\omega\varepsilon} \cdot (\nabla \times \bar{H}) \right] = j\omega\mu_0\bar{\mu}_r\bar{H} \qquad (6.1)$$

where:

σ is the conductor's conductivity [S/m].

ω is the angular frequency [Hz].

ε is the conductor's permittivity [F/m].

$\bar{H}$ is the average magnetic field [A/m].

μ_0 is the permeability of free space (4E-7 H/m).

$\bar{\mu}_r$ is the conductor's average relative permeability [H/m].

Magnetic flux density, forces, torques, losses, and other derived quantities may be calculated from the magnetic field. Ohmic losses in the structure are computed from the induced current [36].

$$P_L = I^2 R \qquad (6.2)$$

where:

P_L is the power loss in a structure [W].

I_L is the induced current in the structure [A].

R is the ohmic resistance [Ω].

6.2   Material Assignment

The coil is for high conductivity reasons made of copper. The heated core is manufactured from CuCrZr (CW106C), which is the same as the hypervapotron sample material. CuCrZr alloy has a strength limit at 450 °C [20]. The side plates are made of S235J steel. The surrounding region was defined as a vacuum because air parameters are nearly identical.

For both CuCrZr and S235J materials bulk (electrical) conductivity is set as temperature dependent – see Figure 33 and Figure .

Except for CuCrZr, all material properties are taken from Maxwell's internal material library.

Table 2: Material definition of copper.

Name	Value	Unit
Relative Permittivity	1	
Relative Permeability	0.999991	
Bulk Conductivity	58 000 000	S/m
Mass Density	8933	kg/m^3
Composition	solid	

Table 3: Material definition of CuCrZr [37].

Name	Value	Unit
Relative Permittivity	1	
Relative Permeability	1	
Bulk Conductivity	43 000 000	S/m
Mass Density	8910	kg/m^3
Composition	solid	
Cp (Specific Heat)	370	J/(kg.K)
Thermal Conductivity	310	W/(m.K)
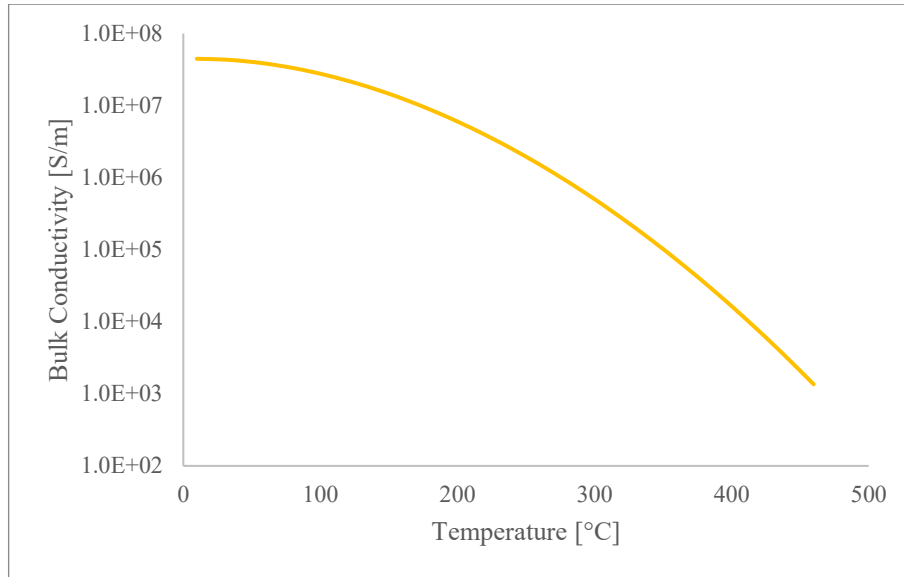
Figure 33: Temperature Dependence of CuCrZr Bulk Conductivity

Table 4: Material definition of steel S235J

Name	Value	Unit
Relative Permittivity	1	
Relative Permeability	1	
Bulk Conductivity	5 434 520	S/m
Mass Density	7 849.9	kg/m^3
Composition	solid	
Cp (Specific Heat)	469.89	J/(kg.K)
Thermal Conductivity	47.917	W/(m.K)
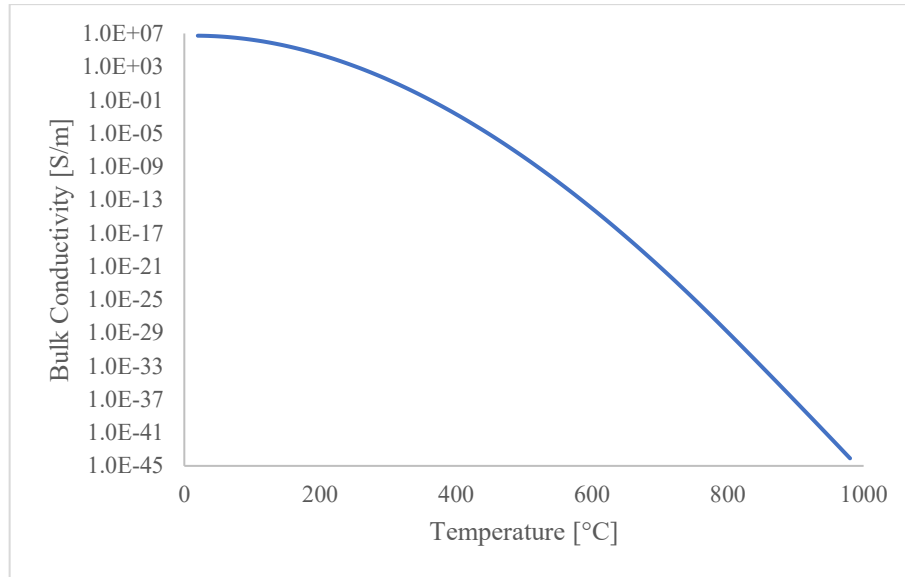
Figure 34}: Temperature Dependence of S235J Bulk Conductivity

Table 5: Material definition of vacuum

Name	Value	Unit
Relative Permittivity	1	
Relative Permeability	0	
Bulk Conductivity	0	S/m
Dielectric Loss Tangent	0	
Magnetic Loss Tangent	0	
Mass Density	0	kg/m^3

6.3   Boundary conditions, excitations

There are no restrictions to the magnetic field generated by the coil on the structure and there is no need to simulate the field going infinitely far. Therefore, the default boundary conditions (Natural and Neumann) are kept. The natural boundary on the structure interfaces means that a magnetic field is continuous there. Neumann boundary on the outer faces of the region surrounding the structures forces the field to be tangential to the boundary and flux cannot cross it [36].

Current excitations of 600 A are assigned to the coil terminals (one of the assignments shown in Figure 34) which are connected to the induction heater. This current is equal to the maximal stated current of the induction heater.
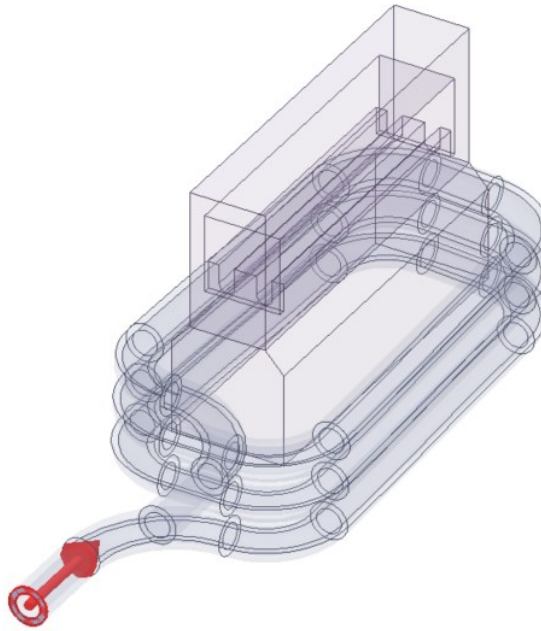
Figure 34: A current excitation assignment on one of the coil terminals

6.4 Mesh definition

As mentioned previously, Maxwell generates the mesh autonomously but accepts mesh construction guidance.

The first mesh operator "On Selection – Skin Depth Based" helps refine the mesh right under the surface where eddy currents are expected as it is visible in Figure 35. Skin Depth is a measure of current concentration at the surface of the selected subject. It is a function of permeability, conductivity, and frequency. This operator is applied to the core surface of Geometry #1 and to the uncovered core surface of Geometry #2 and #3. Also, it is assigned to the steel plates' surface in Geometry #2 and #3.
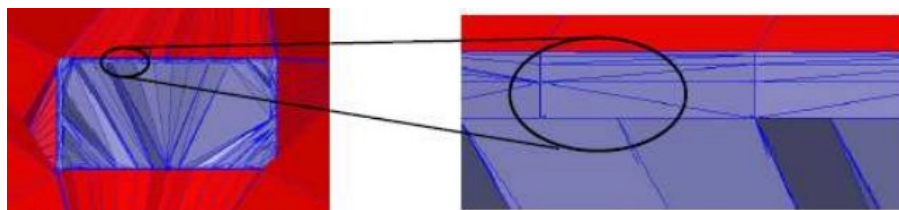
Figure 35: Demonstration of "On Selection - Skin Depth Based" Operator

To increase the density of mesh elements in the whole vacuum region the "Inside Selection – Length based" operator is used and limiting the maximal element size to 60 mm in all geometries.
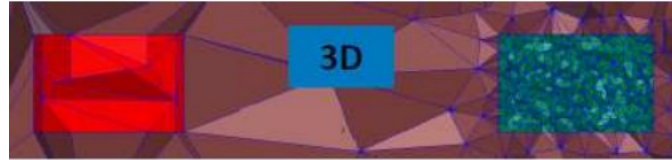
Figure 36: Demonstration of "Inside Selection – Length Based" operator

Surface Approximation control is applied to the coil in all geometries because the mesh would be unnecessarily fine while approximating the rounded shape [36].

6.5   Analysis setup and calculation

In the analysis setup, the simulation frequency of 30 kHz was set. Convergence is controlled by a target Percentage Error of 1 %. It is a delta of energy between two subsequent iterations.

First, Maxwell generates the coarse mesh and calculates the magnetic field, refines the mesh, and calculates the field again. Then it compares the percentage error between two calculations and if the target error is not met it continues with refining and calculations.

7 Fluent Setup

In Ansys Fluent, only the core part and hypervapotron sample are subjected to further analysis. The coil is heating up during the induction heating but has an internal cooling system and therefore does not affect the heating. The water flow in the hypervapotron will be substituted by convective boundary conditions because the simulation of subcooled boiling is not a focus of this work.

7.1 Meshing

The mesh quality significantly affects the accuracy and stability of the computation. The observed attributes are skewness, orthogonal quality, and aspect ratio.

Skewness describes a deviation from a regular cell shape on a scale from 0 (excellent) to 1 (unacceptable). Maximum skewness values should be significantly lower than 0.95. Cells with higher skewness might cause convergence issues and inaccuracy.

Orthogonal quality is an evaluation of angles among the face normal vector, the vector connecting centres of two adjacent cells and the vector from the cell centre to each of the faces. It ranges from 0 (unacceptable) to 1 (excellent). The minimum orthogonal quality of mesh should be substantially higher than 0.02.

Aspect ratio is a measure of the stretching of the cell. Specifically, it is a ratio of the longest cell edge and the shortest cell edge. The value ranges from 1 (excellent) to ∞ (unacceptable). For stable energy solutions, it should be kept below 35 [38].

It was recommended to generate mesh manually through the Outline view mode of Fluent Meshing by Ansys' technical support partner TechSoft Engineering. This common procedure was initially followed but resulted in an unsuccessful electromagnetic loss mapping. Due to that, the simpler Watertight Geometry workflow was applied because it works for simple CAD geometries not requiring mesh clean-up or modifications. The mesh type is polyhedral for all geometries. Above mentioned parameters of generated meshes are listed in Table 6. The meshes seem to be of good quality as they reflect the recommended values.

A notable cell number increase in geometries #2 and #3 is caused by refinement around the added plates.

Table 6: Main parameters of generated meshes

Geometry	Number of cells	Maximum skewness	Minimal orthogonal quality	Aspect ratio
#1	44 573	0.26	0.20	9,5
#2	160 173	0.37	0.28	5,8
#3	168 064	0.36	0.32	7,7
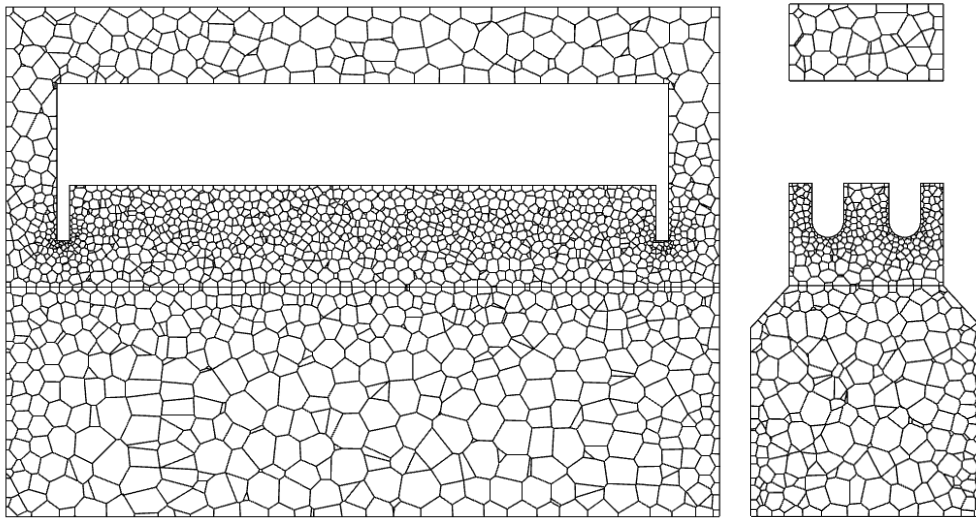
Figure 37: Section view of Geometry #1 mesh
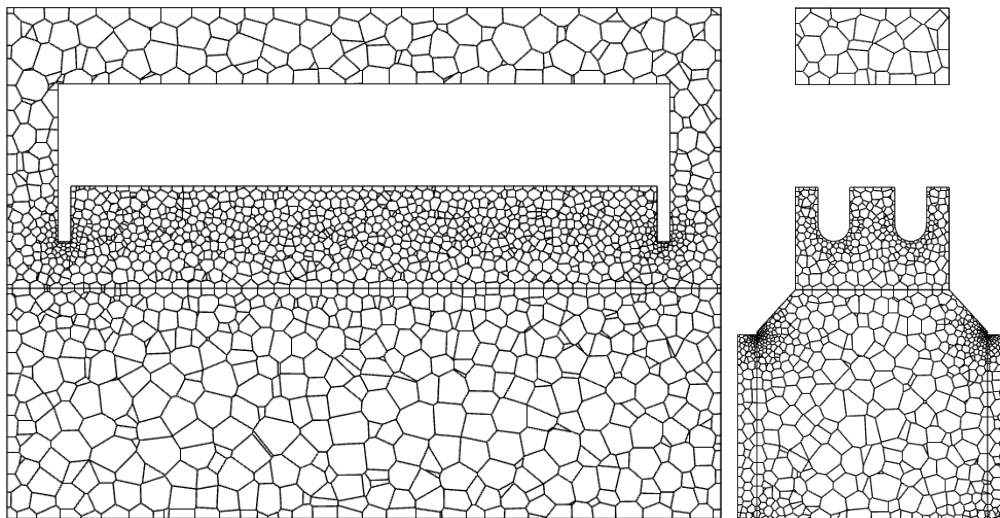
Figure 38 Section view of Geometry #2 mesh
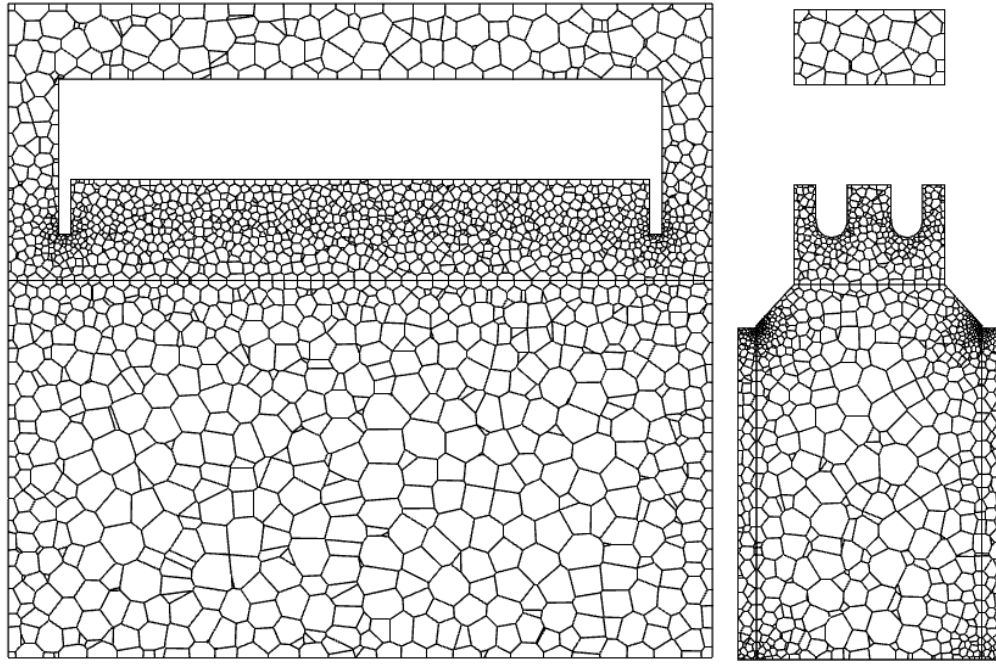
Figure 39 Section view of Geometry #3 mesh

7.2 Model

This simulation needs only an Energy transport equation. Ansys Fluent solves it in the following form:

$$\frac{\partial}{\partial t}\left(\rho(e+\frac{v^2}{2})\right)+\nabla\cdot\left(\rho v(h+\frac{v^2}{2})\right)=\nabla\cdot(k_{eff}\nabla T-\sum_j h_j\vec{J}_j+\bar{\bar{\tau}}_{eff}\cdot\vec{v})+S_h \qquad (7.1)$$

7.3 Material assignment

The same materials as were used in Maxwell were assigned to the geometries in Fluent. The core is CuCrZr and metal plates in Geometries #2 and #3 are defined as steel S235J. Detailed material properties were presented in chapter 6.2

7.4 Boundary conditions

The following tables describe boundary conditions set to the hypervapotron sample and heated geometry. The heated core surface is exposed to room temperature and radiating. For simplification, the convection boundary condition was used with a predefined heat transfer coefficient which approximately corresponds to the radiation.

Table 7 Radiation boundary condition on core surface simplified to convection

Thermal Condition	Convection
Heat transfer coefficient [W/(m²·K)]	20
Free stream temperature [K]	293.15

The outer faces of hypervapotron are insulated from the surroundings and therefore, there is an adiabatic condition.

This thesis is solely focused on the heating and the heat conduction to HV. For that reason, water was substituted by convective boundary conditions on the inner walls of geometries.

The inner part of the hypervapotron consists of surfaces where the water is boiling and where is not. The boiling occurs only on the walls among the fins. The boundary condition setup is in Table 8 and is using heat transfer coefficient of 20 000 W/(m·K) from Milnes' thesis (Figure 40) [15]. The remaining wet surfaces cool down the hypervapotron geometry too but the non-boiling convection (Table 9) is not that efficient in comparison to the subcooled boiling. Thus, 500 W/(m·K) was set as the estimated local heat transfer coefficient. This value will not significantly affect the heat flux from the heated core to HV because it is by two orders of magnitude smaller compared to the one for subcooled boiling.
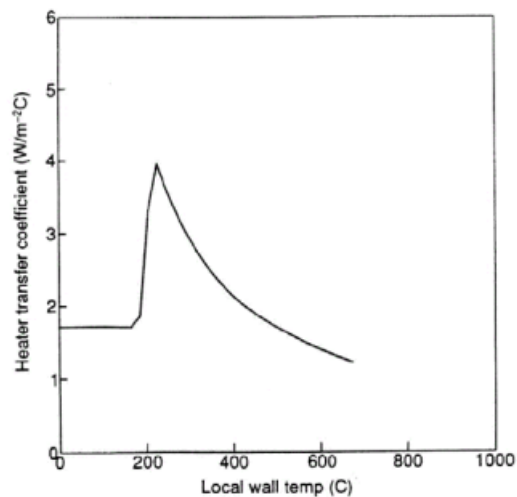

Figure 40 Heat transfer coefficient on the hypervapotron fins while boiling (Milnes [15] assumes there is a typo on the vertical axis and the numbers are 10 000 times higher).

Table 8: Wall boundary condition with boiling.

Thermal Condition	Convection
Heat transfer coefficient [W/(m^2.K)]	20 000
Free stream temperature [K]	432

Table 9: Wall cooling condition without boiling.

Thermal Condition	Convection
Heat transfer coefficient [W/(m^2.K)]	500
Free stream temperature [K]	323.15

The last but very important "boundary condition" or input information for the simulation is the already calculated EM losses which are imported from Maxwell.

7.4.1 Sensitivity analysis for variable heat transfer coefficient

Due to uncertainties about the correct value of the heat transfer coefficient, a simple sensitivity analysis was conducted for Geometry #2. There is a minor heat flux difference between heat transfer coefficients 10 000 and 40 000 W/(m.K) of 2.6 W/m^2 (0.25% increase for higher heat transfer coefficient (HTC)). This means that the exact heat flux coefficient does not have to be known during subcooled boiling with a heat transfer coefficient in the range from 10 000 to 40 000 W/(m.K).

Table 10: Sensitivity analysis for variable HTC

HTC [W/(m.K)]	Free stream temperature [°C]	Heat flux [W/m^2]	Wall temperature [K]
10 000	432	1040,6	512.44
20 000	432	1042,7	477.37
30 000	432	1043,1	464.92
40 000	432	1043,2	458.44
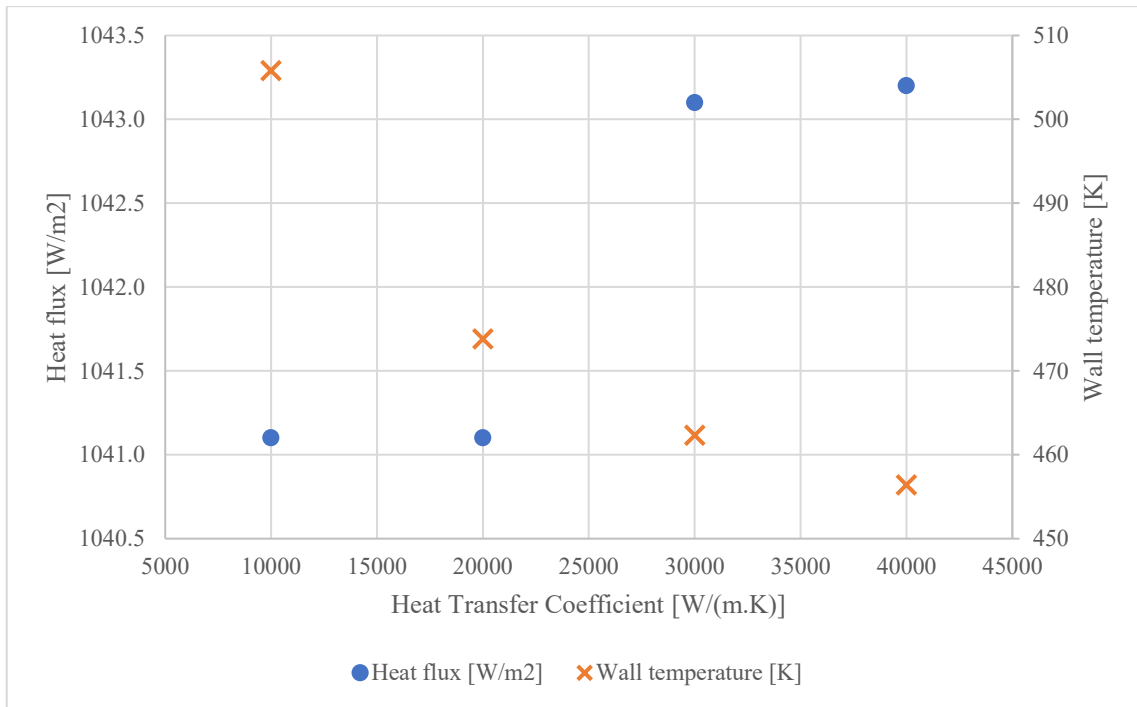
Figure 41: Sensitivity analysis for variable HTC in a plot

7.5 Calculation and convergence monitoring

During simulations energy equations residuals and average temperatures of whole geometries were monitored. It was found that the solutions safely converge in about 25 iterations and the average temperature of the whole geometry was steady too. For the feedback iterator calculations, a buffer of 100 iterations per individual calculation was set up. An example of the residual monitoring from Geometry #1 calculation is in Figure 42. It is also visible that Fluent was calculating only the energy equation. Other residuals were of zero value at all times. That reveals Fluent is not able to provide any calculations for the inviscid flow model and it calculates the heat transfer only with the laminar model.
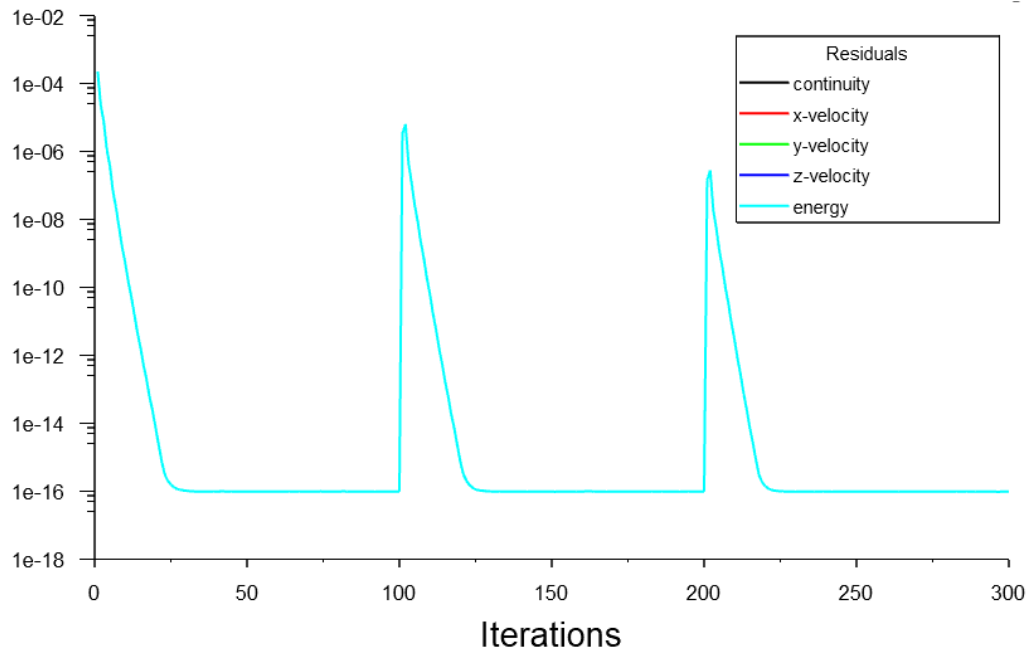
Figure 42: Energy equation residuals of Geometry #1 with three visible feedback iterations.
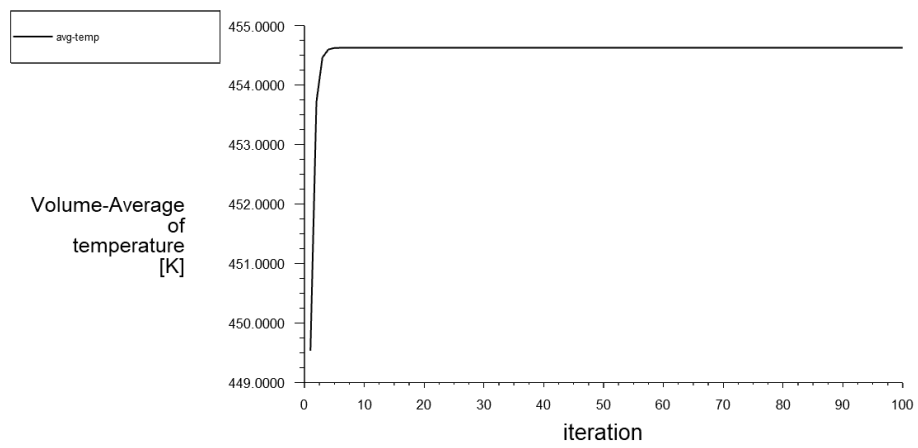
Figure 43: Levelling out of the average temperature of Geometry #1 during the first iteration

8 Results and comments

This chapter presents the key results of simulations for all three geometries. The chapter is divided into two parts, the first showing EM losses in figures, the latter presenting temperature gradients. The results are summarized in Table 11.

Table 11: Overview of losses and heat flux for all geometries

Geometry	Electromagnetic loss [W]	Heat flux [kW/m²]
#1	321.44	458.41
#2	683.71	992.34
#3	753.24	1103.76

8.1 EM Losses

45} shows the EM losses on Geometry #1 which appears to be the biggest ($2.91.10^9$ W/m^3) on the bottom and are almost non-existent (1.95 W/m^3) on the upper core part. In total, the EM loss on Geometry #1 is 321.44 W.
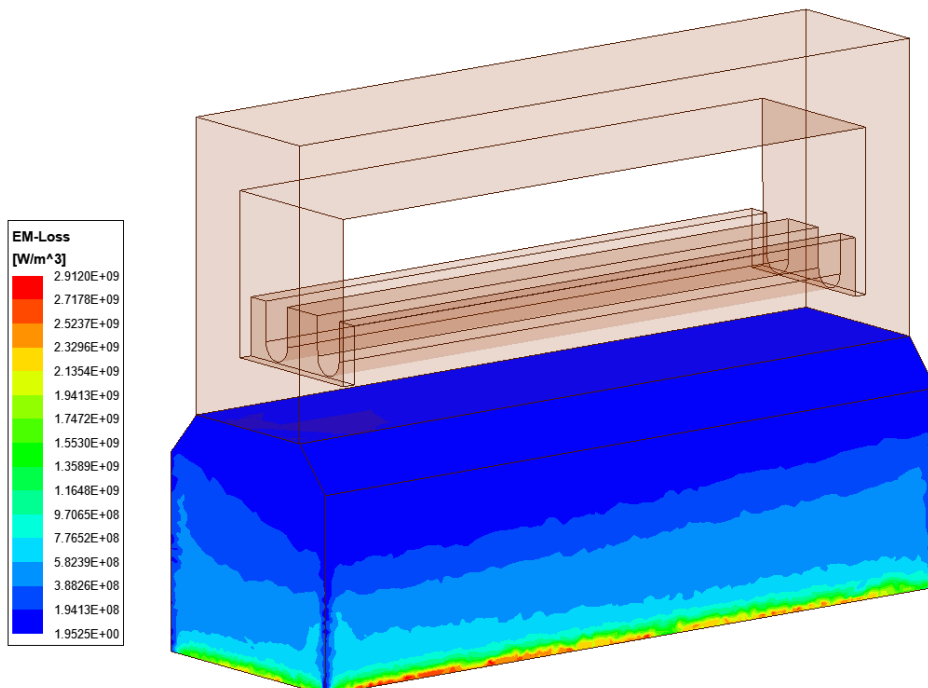
Figure 45}: EM losses on Geometry #1

Figure shows Geometry #2, which was improved by additional steel plates on the sides. EM loss in the entire core part is 683.71 W.
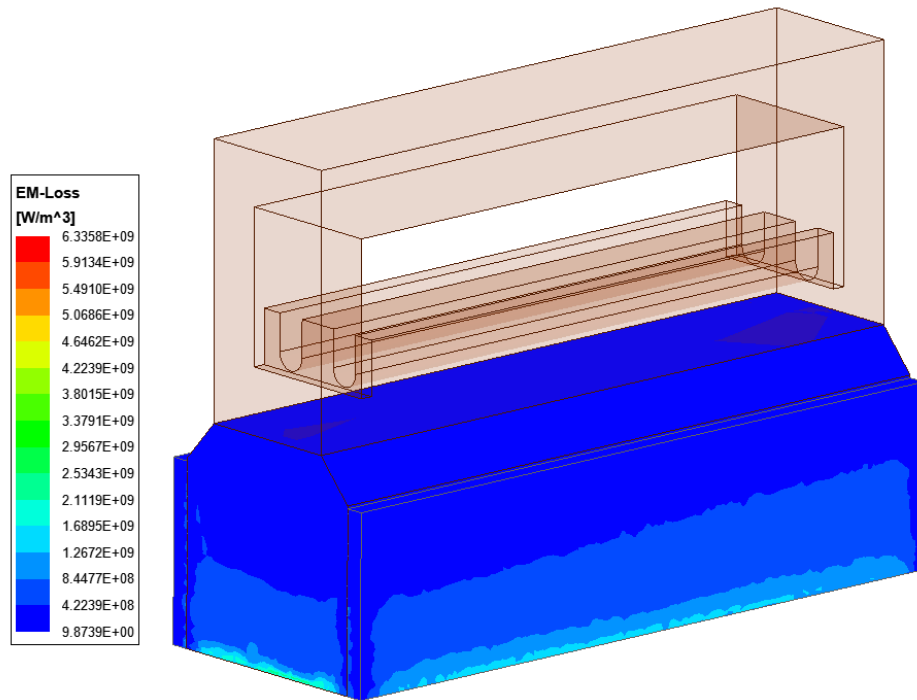
Figure 46}: EM losses on Geometry #2

The last design, Geometry #3, has been lengthened by 11 m to make use of the magnetic field below Geometry #1 and #2. It is visible in Figure that the improvement helped and the total loss also improved by almost 70 W to 753.24 W.
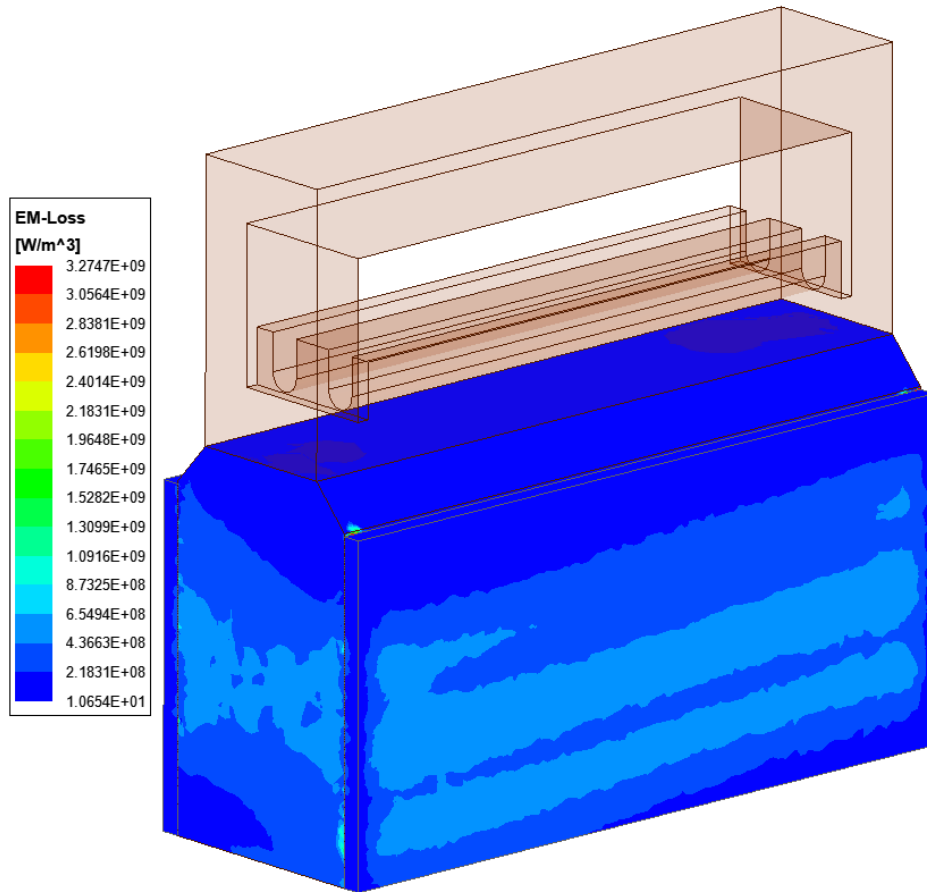
Figure 47}: EM losses on Geometry #3

8.2   Temperature gradients

Figure 44 and Figure 45 capture the resulting temperature gradient from Fluent simulation in section views of Geometry #1. It is visible the highest temperature is in the bottom part of the core where the losses were the largest. The heat flux transferred from the core to the HV is 458.41 W/m². It is calculated on the surface where the core and HV are soldered – the pink line is marking the connection in 28}.
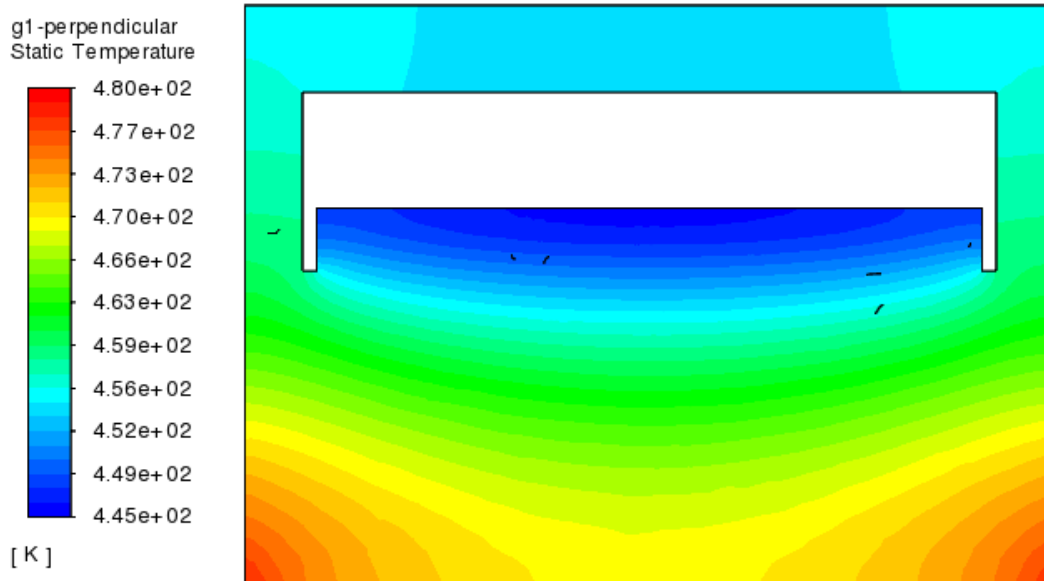
Figure 44: Geometry #1 – Temperature gradient on section view perpendicular to water flow
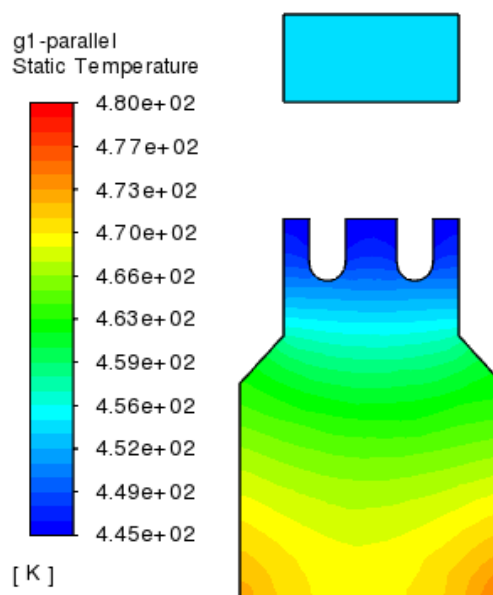
Figure 45: Geometry #1 – Temperature gradient on section view parallel to water flow

Geometry #2 temperature gradient in Figure and Figure 46 is similarly spread but the temperatures are higher. Also, the plates helped to generate more heat. The total heat flux going to the HV is 992.34 W/m^2.
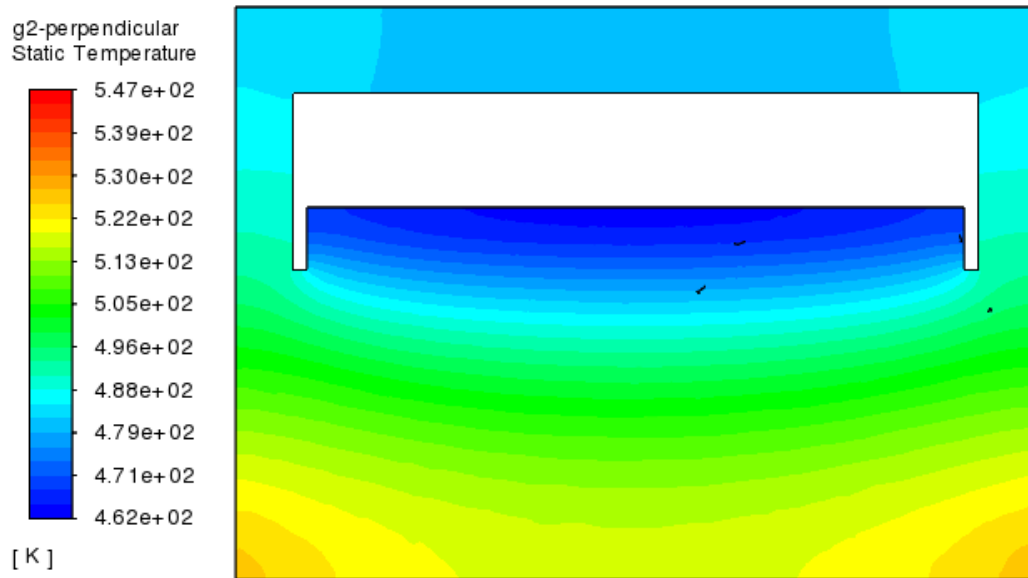
Figure 50}: Geometry #2 – Temperature gradient on section view perpendicular to water flow
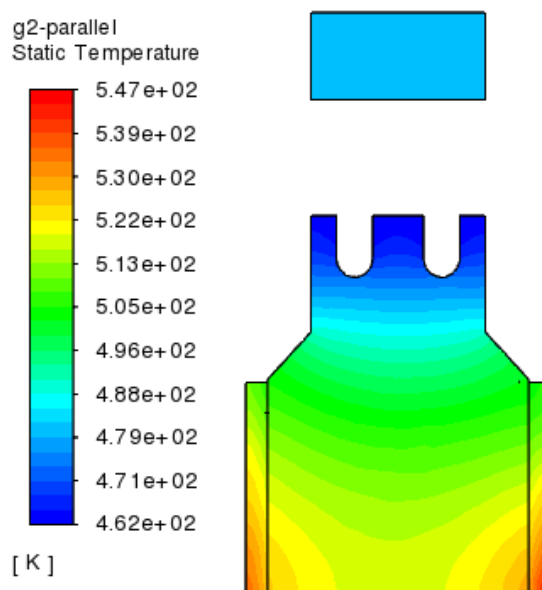
Figure 46: Geometry #2 – Temperature gradient on section view parallel to water flow

Last, Figure and Figure 47 capture the temperature gradient in Geometry #3. These figures clearly show how the core part is heating more than the shorter Geometry #2. The resulting heat flux is the highest from all geometries, 1103.76 W/m².
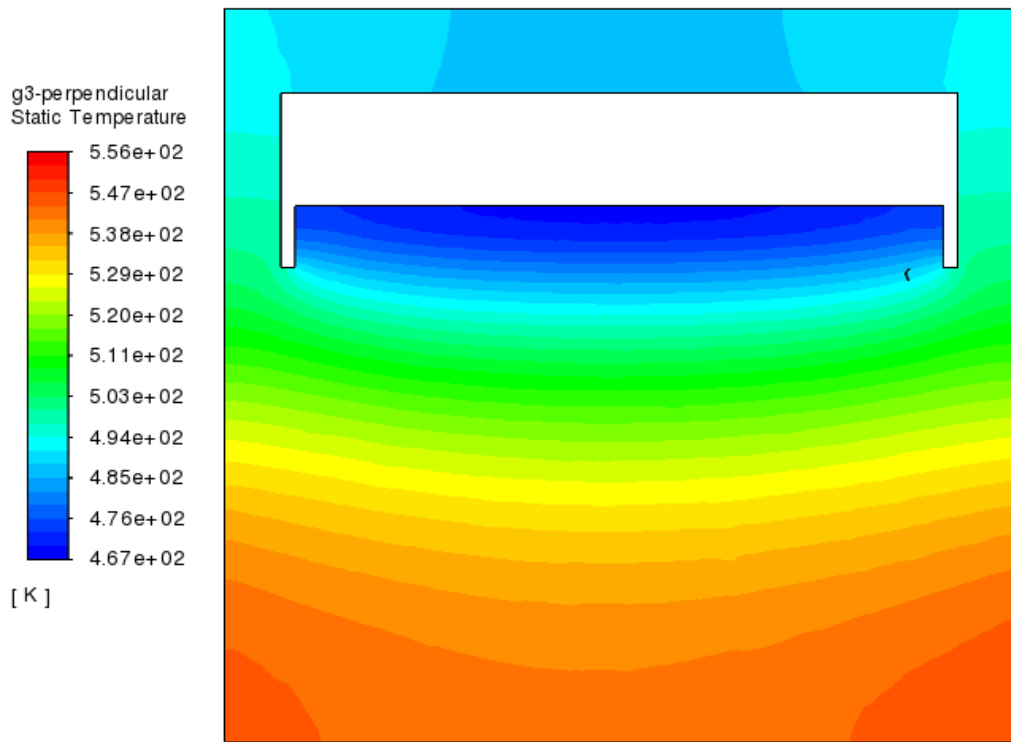
Figure 52}: Geometry #3 – Temperature gradient on section view perpendicular to water flow
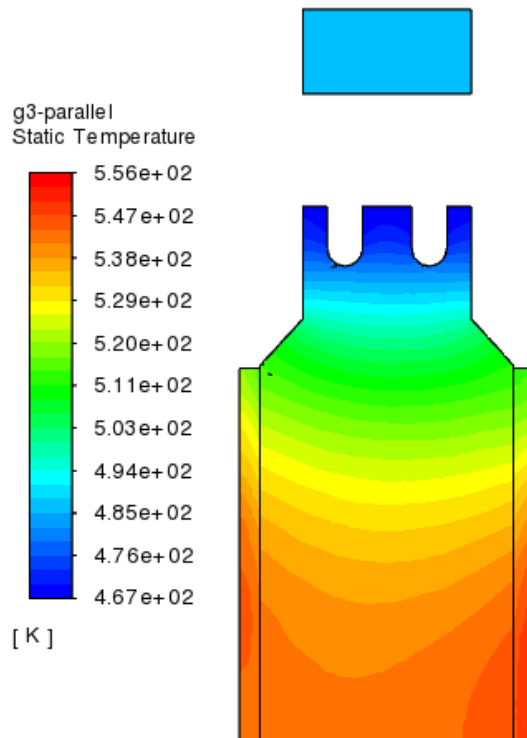
Figure 47: Geometry #3 – Temperature gradient on section view parallel to water flow

All simulated geometries created almost even temperature gradients below HV fins which is practical for accurate HV channel measurements and validation with other researchers.

8.3   Verification with experimental measurements

The original purpose was to simulate and find the best geometry for the induction heating system so that it could be manufactured, installed, and verified on the real experimental hypervapotron sample. Unfortunately, that was not managed until the time of the thesis submission and will be done later.

8.4   Further optimization

A few possible optimization approaches emerged from the research and above-presented results:

1. Eddy-current loss depends on the size and shape of the core. The larger the core, the bigger losses. It would be interesting to scale up the geometry and observe differences because there is still some space under the channel which could be used [31].

2. Eddy-current loss also depends on the resistivity of the magnetic core material. Lower resistivity better allows the needed current flow. Therefore, any future work can take that into account and give a chance to other materials [31].

3. As seen in the figures, losses mostly appear where the coil and its magnetic field are located. To make better use of the magnetic field, the core should be mostly covered by the coil.

Aside from the thesis outcomes, it was proposed to the author to run further research with electrical steel which is used in transformers.

9 Summary

The objective of this thesis is an investigation of the heating system for the experimental sample of hypervapotron.

The research part explains the current technologies for high heat flux cooling in nuclear fusion reactors and how the hypervapotron might be applied as one of the solutions. Hypervapotron is then described in detail including the principle of its operation, history and directly related previous research. Also, the experimental loop is characterized.

The introduction to this topic is followed by an analysis of the thesis assignment. Out of the possible heat sources instead of hot plasma, induction heating was selected and was further simulated using the Ansys software pack. The simulation flow consisted of electromagnetic simulation in Ansys Maxwell, import of EM losses to Ansys Fluent which simulates the heat conduction and a feedback iterator which takes the Fluent results and uses them as input conditions for further iterations of the same simulation steps.

Geometry #1 was initially proposed and therefore simulated as the first. It resulted in 321.44 W EM loss and 458.41 kW/m^2 heat flux conducted to hypervapotron. The first improvement in creating Geometry #2 was the addition of steel plates on the Geometry #1 core sides. This helped and generated a total of 683.71 W in EM loss on the core assembly. The heat flux delivered to the hypervapotron was 992.34 kW/m^2 which is a 116.5% improvement compared to the first geometry. Both Geometry #1 and #2 simulation results showed that most of the heat is generated at the bottom of the designs and therefore Geometry #3 was designed. It is Geometry #2 assembly lengthened by 11 mm to cover possibly unused magnetic field below the geometry. This geometry generated 753.24 W of EM loss and 1103.76 kW/m^2 of heat flux which improved the second geometry heat flux by 11.2 %.

This data will be validated by the real experiment later in a future thesis. In the end, a few optimizations for further research were proposed.

Bibliography

[1]   MALINOWSKI, Leszek, Monika LEWANDOWSKA a Fabio GIANNETTI.
      Design and optimization of the secondary circuit for the WCLL BB option of the
      EU-DEMO power plant. *Fusion Engineering and Design* [online]. 2021, **169** [acc.
      2022-09-03]. ISSN 09203796. Available at: doi:10.1016/j.fusengdes.2021.112642

[2]   FEDERICI, G., L. BOCCACCINI, F. CISMONDI, M. GASPAROTTO, Y.
      POITEVIN a I. RICAPITO. An overview of the EU breeding blanket design
      strategy as an integral part of the DEMO design effort. *Fusion Engineering and
      Design* [online]. 2019, **141**, 30-42 [acc. 2022-09-04]. ISSN 09203796. Available at:
      doi:10.1016/j.fusengdes.2019.01.141

[3]   BARRETT, Thomas, G. ELLWOOD, G. PÉREZ et al. Progress in the engineering
      design and assessment of the European DEMO first wall and divertor plasma facing
      components. *Fusion Engineering and Design* [online]. 2016, **109-111**, 917-924
      [acc.   2022-09-04].   ISSN   09203796.   Available   at:
      doi:10.1016/j.fusengdes.2016.01.052

[4]   HERNÁNDEZ, F., P. PERESLAVTSEV, Q. KANG, P. NORAJITRA, B. KISS, G.
      NÁDASI a O. BITZ. A new HCPB breeding blanket for the EU DEMO: Evolution,
      rationale and preliminary performances. *Fusion Engineering and Design* [online].
      2017, **124**, 882-886 [acc. 2022-09-03]. ISSN 09203796. Available at:
      doi:10.1016/j.fusengdes.2017.02.008

[5]   CISMONDI, F., S. KECSKÉS, M. ILIC et al. Design update, thermal and fluid
      dynamic analyses of the EU-HCPB TBM in vertical arrangement. *Fusion
      Engineering and Design* [online]. 2009, **84**(2-6), 607-612 [acc. 2022-09-03]. ISSN
      09203796. Available at: doi:10.1016/j.fusengdes.2008.12.042

[6]   DEL NEVO, A., E. MARTELLI, P. AGOSTINI et al. WCLL breeding blanket
      design and integration for DEMO 2015: status and perspectives. *Fusion
      Engineering and Design* [online]. 2017, **124**, 682-686 [acc. 2022-09-04]. ISSN
      09203796. Available at: doi:10.1016/j.fusengdes.2017.03.020

[7]   MARTELLI, E., A. DEL NEVO, P. ARENA et al. Advancements in DEMO WCLL breeding blanket design and integration. *International Journal of Energy Research* [online]. 2018, **42**(1), 27-52 [acc. 2022-09-04]. ISSN 0363907X. Available at: doi:10.1002/er.3750

[8]   YOU, J.H., G. MAZZONE, Ch. BACHMANN et al. Progress in the initial design activities for the European DEMO divertor: Subproject "Cassette". *Fusion Engineering and Design* [online]. 2017, **124**, 364-370 [acc. 2022-09-05]. ISSN 09203796. Available at: doi:10.1016/j.fusengdes.2017.03.018

[9]   CHANG, Soon a Won-Pil BAEK. *Understanding, predicting and enhancing Critical Heat Flux: Proceedings of the 10th International Topical Meeting on Nuclear Reactor Thermal Hydraulics (NURETH-10)* [online]. Seoul, Korea, 2003 [acc. 2022-09-16]. Available at: http://thd.ans.org/Awards/tech03/chang_al-01.pdf. Korea Advanced Institute of Science and Technology.

[10] BAXI, C.B. a C.P.C. WONG. Review of helium cooling for fusion reactor applications. *Fusion Engineering and Design* [online]. 2000, **51-52**, 319-324 [acc. 2022-09-06]. ISSN 09203796. Available at: doi:10.1016/S0920-3796(00)00336-7

[11] SCHWARTZ, N, J NICHOLAS, Z JACKSON a P IRELAND. Development of a Novel DEMO divertor target: spiral plate module. *Physica Scripta* [online]. 2021, **96**(12) [acc. 2022-09-06]. ISSN 0031-8949. Available at: doi:10.1088/1402-4896/ac2540

[12] QIAN, X.Y., X.B. PENG, Y.T. SONG et al. New designs of target and cooling scheme for water cooled divertor in DEMO. *Nuclear Fusion* [online]. 2021, **61**(3) [acc. 2022-09-07]. ISSN 0029-5515. Available at: doi:10.1088/1741-4326/abd148

[13] TINCANI, Amelia, Francesca CASTROVINCI, Moreno CUZZANI et al. Hydraulic Characterization of the Full Scale Mock-Up of the DEMO Divertor Outer Vertical Target. *Energies* [online]. 2021, **14**(23) [acc. 2022-09-07]. ISSN 1996-1073. Available at: doi:10.3390/en14238086

[14] YOU, J.H., E. VISCA, T. BARRETT et al. High-heat-flux technologies for the European demo divertor targets: State-of-the-art and a review of the latest testing

campaign. *Journal of Nuclear Materials* [online]. 2021, **544** [acc. 2022-09-06]. ISSN 00223115. Available at: doi:10.1016/j.jnucmat.2020.152670

[15] MILNES, Joseph. *Computational modelling of the HyperVapotron cooling technique for nuclear fusion applications*. Cranfield, 2010. http://dspace.lib.cranfield.ac.uk/handle/1826/5555. Available at: https://dspace.lib.cranfield.ac.uk/handle/1826/5555. Thesis. Cranfield University.

[16] SERGIS, A., Y. HARDALUPAS a T.R. BARRETT. Isothermal velocity measurements in two HyperVapotron geometries using Particle Image Velocimetry (PIV). *Experimental Thermal and Fluid Science* [online]. 2015, **61**, 48-58 [acc. 2022-05-15]. ISSN 08941777. Available at: doi:10.1016/j.expthermflusci.2014.10.003

[17] PÍSEK, Václav. *Verification of CFD methodology applicability to overcooled boiling simulations*. Prague, 2016. Available at: http://hdl.handle.net/10467/66240. Master's thesis. Czech Technical University in Prague.

[18] WANG, Z.W., Y.T. SONG a S.H. HUANG. Analysis and experiment of the hypervapotron mock-up for the EAST upgrade. In: *2011 IEEE/NPSS 24th Symposium on Fusion Engineering* [online]. IEEE, 2011, s. 1-4 [acc. 2022-09-10]. ISBN 978-1-4577-0669-1. Available at: doi:10.1109/SOFE.2011.6052276

[19] CHEN, Peipei. *An Experimental Investigation of Critical Heat Flux Performance of Hypervapotron in Subcooled Boiling*. 2007. Available at: https://hdl.handle.net/2142/85909. Dissertation. University of Illinois at Urbana-Champaign.

[20] CIRIC, D., M. AKIBA, H.-D. FALTER, D. MARTIN, K. SATO a K. YOKOYAMA. Design issues and fatigue lifetime of hypervapotron elements of the JET neutral beam injectors. In: *18th IEEE/NPSS Symposium on Fusion Engineering. Symposium Proceedings (Cat. No.99CH37050)* [online]. IEEE, 1999, s. 407-410 [acc. 2022-09-11]. ISBN 0-7803-5829-5. Available at: doi:10.1109/FUSION.1999.849867

[21] BEURTHERET, Charles A. TRANSFERT DE FLUX SUPERIEUR A lkW/cm2 PAR DOUBLE CHANGEMENT DE PHASE ENTRE UNE PAROI NON ISOTHERME ET UN LIQUIDE EN CONVECTION FORCEE. In: *Proceeding of International Heat Transfer Conference 4* [online]. Connecticut: Begellhouse, 1970, s. 1-11 [acc. 2022-09-16]. Available at: doi:10.1615/IHTC4.420

[22] *Technical Report to JET Contract JC110 VHXX: Application of HyperVapotron Techniques to source of the JET cooling problems*. Thompson CSF, 1980.

[23] CATTADORI, G., G.P. GASPARI, G.P. CELATA, M. CUMO, A. MARIANI a G. ZUMMO. Hypervapotron technique in subcooled flow boiling CHF. *Experimental Thermal and Fluid Science* [online]. 1993, **7**(3), 230-240 [acc. 2022-05-09]. ISSN 08941777. Available at: doi:10.1016/0894-1777(93)90006-5

[24] ESCOURBIAC, Frédéric, J. SCHLOSSER, M. MEROLA a I. BOBIN VASTRA. Experimental optimisation of a hypervapotron® concept for ITER plasma facing components. *Fusion Engineering and Design* [online]. 2003, **66-68**, 301-304 [acc. 2022-05-14]. ISSN 09203796. Available at: doi:10.1016/S0920-3796(03)00172-8

[25] BOBIN-VASTRA, I., F. ESCOURBIAC, M. MEROLA a P. LORENZETTO. Activity of the European high heat flux test facility: FE200. *Fusion Engineering and Design* [online]. 2005, **75-79**, 357-363 [acc. 2022-05-14]. ISSN 09203796. Available at: doi:10.1016/j.fusengdes.2005.08.023

[26] BAXI, C.B. Comparison of swirl tube and hypervapotron for cooling of ITER divertor. In: *Proceedings of 16th International Symposium on Fusion Engineering* [online]. IEEE, 1995, s. 186-189 [acc. 2022-09-16]. ISBN 0-7803-2969-4. Available at: doi:10.1109/FUSION.1995.534199

[27] CHEN, Peipei, Ty NEWELL a Barclay JONES. Heat transfer characteristics in subcooled flow boiling with hypervapotron. *Annals of Nuclear Energy* [online]. 2008, **35**(6), 1159-1166 [acc. 2022-09-16]. ISSN 03064549. Available at: doi:10.1016/j.anucene.2007.01.015

[28] GLEITZ, M., P. ZÁCHA, S. ENTLER a J. SYBLÍK. *DESIGN OF EXPERIMENTAL DEVICE FOR TESTING OF SUBCOOLED FLOW BOILLING* [online]. In: . s. 150-153 [acc. 2022-09-16]. Available at: doi:10.21495/5896-3-150

[29] BAE, Young-Dug, Suk-Kwon KIM, Dong-Won LEE, Hee-Yun SHIN a Bong-Guen HONG. Development of a High Heat Load Test Facility KoHLT-1 for a Testing of Nuclear Fusion Reactor Components. *Journal of the Korean Vacuum Society* [online]. 2009, **18**(4), 318-330 [acc. 2022-09-16]. ISSN 1225-8822. Available at: doi:10.5757/JKVS.2009.18.4.318

[30] PROKŮPEK, Jan, Karel SAMEC, Richard JÍLEK, Pierre GAVILA, Soběslav NEUFUSS a Slavomír ENTLER. HELCZA—High heat flux test facility for testing ITER EU first wall components. *Fusion Engineering and Design* [online]. 2017, **124**, 187-190 [acc. 2022-09-16]. ISSN 09203796. Available at: doi:10.1016/j.fusengdes.2017.03.059

[31] KAZIMIERCZUK, Marian K. *High-frequency magnetic components*. 2nd ed. Chichester: Wiley, 2014. ISBN 978-111-8717-790.

[32] LUCIA, Oscar, Pascal MAUSSION, Enrique DEDE a Jose BURDIO. Induction Heating Technology and Its Applications: Past Developments, Current Technology, and Future Challenges. In: *IEEE Transactions on Industrial Electronics* [online]. 2014, , s. 2509-2520 [acc. 2022-05-25]. ISSN 0278-0046. Available at: doi:10.1109/TIE.2013.2281162

[33] Ansys Maxwell. In: *Virtuální prototypování v Ansys | TechSoft Engineering* [online]. [acc. 2022-05-12]. Available at: https://www.techsoft-eng.cz/software/ansys-maxwell

[34] ANSYS Fluent. In: *SVS FEM* [online]. SVS FEM [acc. 2022-06-10]. Available at: https://www.svsfem.cz/produkty/proudeni/ansys-fluent

[35] Ansys Workbench. In: *Virtuální prototypování v Ansys | TechSoft Engineering* [online]. TechSoft Engineering [acc. 2022-05-12]. Available at: https://www.techsoft-eng.cz/software/ansys-workbench

[36] ANSYS, INC. *Maxwell Help: Release 2021 R1*. Canonsburg, 2021.

[37] CuCr1Zr, C18150 | Datasheet. In: *METALCOR* [online]. METALCOR [acc. 2022-09-16]. Available at: http://www.metalcor.de/en/datenblatt/133/

[38] *Ansys Fluent User's Guide*. Release 2021 R2. U.S.A.: ANSYS, Inc, 2021.